

Contents lists available at ScienceDirect

Mechanics of Materials

journal homepage: www.elsevier.com/locate/mechmat



Extended isogeometric analysis for dynamic fracture in multiphase piezoelectric/piezomagnetic composites

Tinh Quoc Bui^{a,*}, Sohichi Hirose^a, Chuanzeng Zhang^b, Timon Rabczuk^c, Cheng-Tang Wu^d, Takahiro Saitoh^e, Jun Lei^f

^a Department of Mechanical and Environmental Informatics, Tokyo Institute of Technology, 2-12-1-W8-22, O-okayama, Meguro-ku, Tokyo 152-8552, Japan

^b Department of Civil Engineering, University of Siegen, Paul-Bonatz-Str. 9-11, Siegen 57076, Germany

^c Institute of Structural Mechanics, Bauhaus University Weimar, 99423 Weimar, Germany

^d Livermore Software Technology Corporation, 7374 Las Positas Road, Livermore, CA 94551, USA

^e Department of Civil and Environmental Science, Gunma University, 1-5-1-413, Tenjin, Kiryu, Gunma, Japan

^f Department of Engineering Mechanics, Beijing University of Technology, Beijing 100124, PR China



ARTICLE INFO

Article history:

Received 13 August 2015

Revised 29 January 2016

Available online 10 March 2016

Keywords:

Magnetoelastic
Isogeometric analysis
Dynamic fracture
XIGA
XFEM
Smart materials

ABSTRACT

A dynamic extended isogeometric analysis (XIGA) is developed for transient fracture of cracked magnetoelastic (MEE) solids under coupled electro-magneto-mechanical loading, taking the advantages of high order NURBS basis functions and enrichment methods. The extended dynamic fracture parameters are estimated through the electro-magneto-mechanical interaction integral. Numerical examples of electrically and magnetically impermeable cracks are studied to demonstrate the accuracy of the proposed XIGA and its ability in reproducing important phenomenological characteristics and behaviors of transient dynamic cracks in MEE materials. Our main objective focuses on the numerical investigations of transient dynamic cracks computed by the XIGA, investigating the effects of some numerical aspects on the responses, presenting new numerical results of dynamic responses, and addressing the XIGA performance. Different degrees of NURBS, polarization, finite size effects, enrichments, loadings, multiple cracks, volume fraction, different multiphase compositions of piezoelectric/piezomagnetic, etc. affecting the responses are investigated. Illustration of scattered elastic waves propagating in the cracked MEE is depicted to take an insight look at the behavior of responses.

© 2016 Elsevier Ltd. All rights reserved.

1. Introduction

The modern smart materials are being widely applied to many industrial areas including biomedical devices, automotive, aerospace, microelectromechanical and nanoelectromechanical systems, civil engineering. In particular the multiphase magnetoelectroelastic (MEE) composite materials (Nam, 1994), which consist of piezomagnetic and piezoelectric phases, have extensively used in areas such as sensors, actuators, transducers, medical ultrasonic

imaging devices, and so on, as a result of the inherent coupling effects among mechanical, electric and magnetic fields. One of the most popular examples of MEE material is the CoFe_2O_4 - BaTiO_3 composite, which is made of a piezomagnetic Cobalt Ferrite – CoFe_2O_4 phase as matrix material and a piezoelectric Barium Titanate – BaTiO_3 phase as embedded material (Nam, 1994; Corral-Flores et al., 2010). It is well known that the CoFe_2O_4 - BaTiO_3 composites behave very brittle. Therefore, a numerical fracture analysis of CoFe_2O_4 - BaTiO_3 composites based on the linear elastic fracture mechanics becomes important for the development of this type of smart structures.

Under loading conditions in-service and during the manufacturing process, the imperfection or defects like

* Corresponding author. Tel.: +81 7021506399.
E-mail address: tinh.buiquoct@gmail.com (T.Q. Bui).

cracks may occur and greatly affect the integrity of the materials and the performance of the structures. A thorough interpretation and better understanding of fracture behaviors of cracked MEE composites under coupled electro-magneto-elastic impact loadings is hence essential to the structural design of smart devices.

Over the past few decades there have been extensive studies and investigations on the fracture modeling of MEE media, and the corresponding numerical approaches have thus been developed. However, an efficient and accurate fracture modeling of MEE media, especially under the dynamic impact loading, remains challenging in computational fracture mechanics. The challenges lie in the complexity of the numerical and mathematical modeling including, the anisotropic behaviors of multiphase materials, the inherent coupling effects among the magnetic, electric and mechanic fields, and the complex situation of the dynamic impact loading. It is our attempt in this work to present an efficient numerical approach, which is based on the extended isogeometric analysis enhanced by enrichments and associated with the NURBS (non-uniform rational B-spline) basis functions, to accurately model the transient dynamic cracks in multiphase MEE materials under the coupled time-dependent loading condition.

The dynamic fracture behavior of MEE structures is a crucial issue in engineering applications and material sciences as its result often has a direct relevance to the optimization and the design of the engineering devices and structures (Wünsche et al., 2012). While most of the preceding works have been devoted to the modeling of crack problems under the static loading conditions, the studies under the dynamic loading are still rare. In terms of theoretical analyses, Feng et al. (2007) and Feng and Pan (2008) respectively analyzed the dynamic fracture of a penny-shaped crack in a MEE layer and an internal interfacial crack between two dissimilar MEE plates using singular integral equations and transformation methods as Laplace, Hankel and Fourier techniques; Zhong et al. (2009a,b) also adopted the Laplace, Fourier transforms and singular integral equation with Cauchy kernel to study transient response of a cracked MEE and two collinear dielectric cracks under impacts; Zhou et al. (2005) analyzed the dynamic results for two collinear interface cracks in MEE materials; and among others. Nevertheless, solutions based on the analytical approaches are available only for problems with simple crack configuration and boundary and loading conditions. Therefore it is in a great need for the development of advanced numerical methods for practical and more general problems.

Most of the published works dealing with cracked MEE media under dynamic impact loading are based on the boundary element method (BEM), e.g., see Lei et al. (2015), Rojas-Diaz et al. (2011), Rojas-Diaz et al. (2008), Rojas-Diaz et al. (2009), Rojas-Diaz et al. (2010), Wünsche et al. (2013), and Lei et al. (2015). A very few works of dynamic crack analysis are derived either from the meshless methods (Sladek et al., 2008; Sladek et al., 2010; Sladek et al., 2012) or the extended finite element method (XFEM) (Bui and Zhang, 2013), while some other studies using the conventional finite element method (FEM) or its coupling with the meshless MLPG, e.g., see Wang and Mai (2007) and

Li et al. (2009), are developed for the static analysis. Although the meshfree methods (e.g., see Sladek et al., 2008; Sladek et al., 2010; Sladek et al., 2012; Bui et al., 2011; Nguyen et al.; 2014; Racz and Bui; 2012; Bui et al., 2013) have found to be potential and effective for solving some particular engineering problems including the modeling of cracks, one of their major disadvantages, which has substantially restricted their applications in practices, lies in the high computational costs. The meshing issues in traditional FEM and the BEM make them very time-consuming and ineffective in dealing with crack problems. In BEM, finding an appropriate fundamental solution for practical problems is often not trivial. Additionally, the complexity of mathematical expressions and formulation because of using integral equations makes the BEM to be cumbersome. The BEM in general is useful but limited to a certain types of problems. The XFEM using enrichment techniques, e.g., see Bui and Zhang (2013) and Bui and Zhang (2012), has shown many great advantages over the traditional FEM and BEM in the simulation of crack problems such as, the crack geometry modeled by the XFEM is independent of the mesh; re-meshing in crack propagation is no longer required; the accuracy of solutions for non-smoothed problems is high, and so forth. The authors have recently developed and successfully applied several XFEM techniques to solve some engineering problems including dynamic and static crack analysis of piezoelectric materials (Bui and Zhang, 2012; Sharma et al., 2013; Liu et al., 2013; Liu et al., 2014; Yu et al., 2015); buckling analysis of cracked functionally graded materials plates (Liu et al., 2015), fatigue crack growth in FGM plates (Bhattacharya et al., 2013), vibration analysis of cracked Reissner–Mindlin plates (Yu et al., 2016a), and cohesive crack growth in concrete structures (Zhang and Bui, 2015).

It is well known that the original idea of the isogeometric analysis (IGA) (Hughes et al., 2005) is to integrate between the analysis and design. The IGA generally is to overcome or reduce the errors induced by the approximation of geometries, which almost encounters in traditional numerical approaches using different basis shape functions for the geometric discretization and unknown field approximation. The concept of IGA using the NURBS in computer-aided-design (CAD) is pioneered by Hughes et al. (2005). The key idea behind the IGA lies in the fact that the IGA employs the complex NURBS basis functions in the finite element analysis application directly, which means that the same NURBS basis functions used for the construction of geometric representation are taken to discretize the field variable solutions. As stated in Cottrell et al. (2009), essentially it allows the models of interest to be designed, adjusted and tested in one go using a common data set, and this fact apparently makes the IGA approach different from the conventional FEM. In addition, the high order continuity of the basis functions, high accuracy, and especially the accuracy can be controllable are also some other advantages of the IGA over the conventional methods. Nowadays the IGA is a useful and potential numerical tool as it has been applied to solve a wide range of engineering problems. Relevant references for the developments and applications of the IGA are not mentioned here due to the sake of brevity but they can be found in the literature easily

and effortlessly. Since the IGA inherently owns many advantages over the classical methods, and in light of its developments, the authors recently have applied the IGA to solve some interesting problems including linear and non-linear structural mechanics (Yu et al., 2015; Yin et al., 2014; Yin et al., 2015; Yin et al., 2015; Shojaee et al., 2012; Valizadeh et al., 2013; Valizadeh et al., 2013), and porous media (Nguyen et al., 2014). We have observed that since the IGA allows for the higher global regularity of the NURBS basis functions, attaining higher accuracy on the solutions is thus possible. We will later illustrate this desirable feature in the numerical results.

In recent years, the combination of the IGA and the enrichment method (XFEM) is developed for dealing with non-smoothed problems like cracks or material interfaces (Benson et al., 2010; De Luycker et al., 2011; Yu et al., 2016c; Ghorashi et al., 2011), taking advantages of the strengths and making use all the desirable characteristics of both techniques. Later on, the method is termed as the XIGA. Consequently, major features of the NURBS based XIGA can be summarized as follows: (a) bridging the gap between the analysis and design; (b) overcoming the errors arisen from the geometric discretization; (c) precisely capturing the singularity and the discontinuity induced by cracks; (d) modeling moving boundaries or the evolution of cracks without re-meshing; (e) the accuracy of the solutions is high; and many others. The development stage of the XIGA for practical or other complex engineering problems is still very young as there exist very few works just recently published, for instance, crack growth in 2D elastic solids (Ghorashi et al., 2011), static and dynamic transient analysis of cracked piezoelectric materials (Bui, 2015), thermal buckling analysis of functionally graded plates with internal defects (Yu et al., 2016b); stochastic fatigue life prediction of interface crack in bi-layered graded materials (Bhardwaj et al., 2015), cracked orthotropic composites (Ghorashi et al., 2015), and functionally graded cracked plates under different loads and boundary conditions (Bhardwaj et al., 2015).

In this paper, we present for the first time an extension of the XIGA to model transient dynamic cracks of multiphase MEE composites under the coupled magneto-electro-mechanical impact loading. We aim to numerically investigate the transient dynamic responses of 2D, homogeneous, anisotropic and linear cracked MEE solids calculated by the developed dynamic XIGA. An implicit time integration scheme is hence developed. The eight-fold magneto-electro-mechanical branch enrichment functions are adopted to better capture the singular fields at the crack tip in MEE materials. The pure mechanical fourfold branch functions used in isotropic elastic materials are also examined to show the influence of the pure enrichment functions on the transient responses in dynamic crack analysis. In addition, the discontinuous Heaviside function is employed to represent the discontinuities across the crack faces far away from the crack tip.

In dynamic XIGA modeling, the governing equations of initial-boundary value problem for cracks are transformed into the weak form, and the resulting time-dependent system of discrete equations is then solved by the implicit

Newmark time integration scheme. In this work, the path-dependent magnetoelectromechanical J -integral is taken to extract the extended dynamic intensity factors. For the MEE composites being studied in this work, and unlike isotropic solids, the extended dynamic fracture parameters are characterized through the dynamic mechanical stress intensity factors (DSIF) K_{II} , K_I , the dynamic electrical displacement intensity factor (DEDIF) K_{IV} , and the dynamic magnetic induction intensity factor (DMIIIF) K_V .

To show the accuracy and performance of the developed method, three numerical examples of electrically and magnetically impermeable cracks including a central crack, an inclined edge cracked and two equal parallel cracks in MEE plates are considered. The present numerical results of the dynamic extended intensity factors are validated versus reference solutions obtained from other numerical methods such as the BEM and XFEM. The mixed-mode fractures in anisotropic MEE materials can easily be captured by altering the orientation of the material poling direction. We numerically address the variation of the transient responses accounted for different orders of the NUBRS basis functions. The influences of different enrichment functions, polarization direction, finite size effect, intensity of the magneto-electro-mechanical loading, volume fraction, etc. on the extended dynamic fracture parameters are numerically explored. In addition, the transient responses of the normalized dynamic intensity factors accounting for different multiphase compositions of piezoelectric/piezomagnetic using the developed XIGA are considered. Illustration of scattered elastic waves propagating in the cracked MEE structures is also depicted schematically for further interpreting the behaviors of the transient responses computed.

The body of this paper starts with the governing equations of anisotropic MEE materials. We then detail in Section 2 the dynamic XIGA formulation applied to dynamic cracked MEE problems, in which the NUBRS basis functions, the enriched isogeometric finite element approximation, the partition of unity branch functions suitable for MEE materials, discrete equations, and numerical integration are presented. In Section 3, the computation of extended dynamic fracture parameters is briefly given. Three numerical examples are considered and the computed numerical results are then presented and discussed in Section 4. Some conclusions drawn from the study are given in Section 5.

2. Governing equations of magnetoelectroelastic materials

2.1. Field equations

Let us consider a 2D homogeneous, linear and anisotropic magnetoelectroelastic (MEE) solid. In a 2D Cartesian coordinate system, the field equations involving the generalized constitutive equations, kinematic equations and equilibrium equations in the presence of body forces f_i^{mech} , electric body charges f_i^{elec} , magnetic body currents f_i^{mag} and under the quasi-static assumption for the electromagnetic fields take the form (Wünsche et al., 2012; Lei et al., 2015; Rojas-Diaz et al., 2011; Bui and Zhang, 2013)

$$\begin{aligned}\sigma_{ij} &= C_{ijkl}\varepsilon_{kl} - e_{lij}E_l - h_{lij}H_l; \\ D_i &= e_{ikl}\varepsilon_{kl} + \kappa_{il}E_l + \beta_{il}H_l; \\ B_i &= h_{ikl}\varepsilon_{kl} + \beta_{il}E_l + \gamma_{il}H_l\end{aligned}\quad (1)$$

$$\varepsilon_{ij} = \frac{1}{2}(u_{i,j} + u_{j,i}), \quad E_i = -\phi_{,i}, \quad H_i = -\varphi_{,i} \quad (2)$$

$$\sigma_{ij,j} + f_i^{\text{mech}} = \rho\ddot{u}_i, \quad D_{i,i} = f_i^{\text{elec}}, \quad B_{i,i} = f_i^{\text{mag}} \quad (3)$$

where C_{ijkl} , κ_{il} and γ_{il} are the elastic stiffness tensor, the dielectric permittivities and the magnetic permeabilities, whereas e_{lij} , h_{lij} and β_{il} are the piezoelectric, piezomagnetic and electromagnetic coupling coefficients, respectively. σ_{ij} , ε_{ij} , D_i , E_i , B_i and H_i are the mechanical stress tensor, mechanical strain tensor, electric displacement vector, electric field vector, magnetic induction vectors, and magnetic field vector, respectively. Also, u_i , ϕ and φ denote the elastic displacements, scalar electric potential, and magnetic potential, respectively. In Eq. (3), \ddot{u}_i denotes the second time derivative of the displacements, and ρ is the mass density. The following reciprocal symmetries hold

$$\begin{aligned}C_{ijkl} &= C_{jikl} = C_{ijlk} = C_{lkij}, \quad e_{kij} = e_{kji}, \quad h_{kij} = h_{kji}, \\ \kappa_{ij} &= \kappa_{ji}, \quad \beta_{ij} = \beta_{ji}, \quad \gamma_{ij} = \gamma_{ji}\end{aligned}\quad (4)$$

2.2. Boundary and initial conditions

A MEE body containing a traction-free crack $\Gamma_C = \Gamma_C^- \cup \Gamma_C^+$ occupies a domain $\Omega \subset \Re^2$ bounded by its boundary Γ with an outward unit normal vector n_i . In the initial-boundary value problems, the primary field variables u_i , ϕ , φ and σ_{ij} , D_i , and B_i , respectively, satisfy the following essential and natural boundary conditions

$$u_j = \bar{u}_j \text{ on } \Gamma_u, \quad \phi = \bar{\phi} \text{ on } \Gamma_\phi, \quad \phi = \bar{\phi} \text{ on } \Gamma_\phi \quad (5)$$

$$\begin{aligned}\sigma_{ij}n_j &= \bar{t}_j^{\text{mech}} \text{ on } \Gamma_\sigma, \quad D_jn_j = \bar{t}_j^{\text{elec}} \text{ on } \Gamma_D, \\ B_jn_j &= \bar{t}_j^{\text{mag}} \text{ on } \Gamma_B\end{aligned}\quad (6)$$

where Γ_u , Γ_ϕ and Γ_φ , respectively, are the essential boundaries prescribed by the displacements, electric potential, and magnetic potential, while Γ_σ , Γ_D and Γ_B , respectively, are the natural boundaries imposed by the tractions, electric displacements, and the magnetic inductions. They are disjointed such that $\Gamma_u \cup \Gamma_\sigma = \Gamma$ or $\Gamma_D \cup \Gamma_\phi = \Gamma$ or $\Gamma_B \cup \Gamma_\varphi = \Gamma$. In Eqs. (5) and (6), an over-bar represents the prescribed values. Throughout the study, the crack faces Γ_C are assumed to be traction-free and electrically and magnetically impermeable, i.e.,

$$\sigma_{ij}n_j = 0, \quad D_jn_j = 0, \quad B_jn_j = 0 \quad \text{on } \Gamma_C \quad (7)$$

The initial conditions at time $t = 0$ are specified as

$$u_i(t = 0) = \bar{u}_i(0), \quad \dot{u}_i(t = 0) = \dot{\bar{u}}_i(0) \quad (8)$$

where \bar{u}_i and $\dot{\bar{u}}_i$ are the initial displacements and velocities, respectively.

2.3. Complex crack-tip fields in magnetoelectroelasticity

Based on the generalized Stroh's formalism for anisotropic elasticity, the near-tip mechanical displacements, the electrical potential and the magnetic potential

for cracked homogeneous transversely isotropic MEE solid are expressed in polar coordinates $(\hat{r}, \hat{\theta})$ with the origin at the crack-tip (Bui and Zhang, 2013; Rao and Kuna, 2008)

$$\begin{aligned}u_i(\hat{r}, \hat{\theta}) &= \sqrt{\frac{2\hat{r}}{\pi}} \sum_N K_N d_i^N(\hat{\theta}), \\ \phi(\hat{r}, \hat{\theta}) &= \sqrt{\frac{2\hat{r}}{\pi}} \sum_N K_N v^N(\hat{\theta}), \\ \varphi(\hat{r}, \hat{\theta}) &= \sqrt{\frac{2\hat{r}}{\pi}} \sum_N K_N w^N(\hat{\theta})\end{aligned}\quad (9)$$

and the mechanical stresses, the electrical displacements and the magnetic inductions are given by

$$\begin{aligned}\sigma_{ij}(\hat{r}, \hat{\theta}) &= \frac{1}{\sqrt{2\pi\hat{r}}} \sum_N K_N f_{ij}^N(\hat{\theta}), \\ D_i(\hat{r}, \hat{\theta}) &= \frac{1}{\sqrt{2\pi\hat{r}}} \sum_N K_N g_i^N(\hat{\theta}), \\ B_i(\hat{r}, \hat{\theta}) &= \frac{1}{\sqrt{2\pi\hat{r}}} \sum_N K_N q_i^N(\hat{\theta})\end{aligned}\quad (10)$$

It is obvious that the fields of mechanical stresses, electrical displacements and magnetic inductions at the crack-tip exhibit the traditional square root singularities (Rao and Kuna, 2008). In Eq. (10), $i, j=1, 2$ and the summation over $N = II, I, III, IV, V$ comprises the mechanical stress intensity factors, K_{II} , K_I , K_{III} , (note that K_{III} is zero for 2D in plane case), the electric displacement intensity factor, K_{IV} , and the magnetic induction intensity factor, K_V . The standard angular functions $f_{ij}^N(\hat{\theta})$, $g_i^N(\hat{\theta})$, $q_i^N(\hat{\theta})$, $d_i^N(\hat{\theta})$, $v^N(\hat{\theta})$ and $w^N(\hat{\theta})$ for a homogeneous and linear cracked MEE medium are depending on the material properties. In particular, they can be expressed in terms of complex eigenvalues p_ω , eigenvectors $\tilde{A}_{M\omega}$ and matrices $\tilde{N}_{\omega N}$ and $\tilde{M}_{M\omega}$, using the generalized Stroh's formalism and semi-analytical calculations as (Bui and Zhang, 2013; Rao and Kuna, 2008; Song and Sih, 2003)

$$\begin{aligned}f_{i1}^N &= - \sum_{\omega=1}^5 \text{Re} \left\{ \frac{\tilde{M}_{i\omega} \tilde{N}_{\omega N} p_\omega}{\sqrt{\cos \hat{\theta} + p_\omega \sin \hat{\theta}}} \right\}, \\ f_{i2}^N &= \sum_{\omega=1}^5 \text{Re} \left\{ \frac{\tilde{M}_{i\omega} \tilde{N}_{\omega N}}{\sqrt{\cos \hat{\theta} + p_\omega \sin \hat{\theta}}} \right\}; \\ g_1^N &= - \sum_{\omega=1}^5 \text{Re} \left\{ \frac{\tilde{M}_{4\omega} \tilde{N}_{\omega N} p_\omega}{\sqrt{\cos \hat{\theta} + p_\omega \sin \hat{\theta}}} \right\}, \\ g_2^N &= \sum_{\omega=1}^5 \text{Re} \left\{ \frac{\tilde{M}_{4\omega} \tilde{N}_{\omega N}}{\sqrt{\cos \hat{\theta} + p_\omega \sin \hat{\theta}}} \right\}; \\ q_1^N &= - \sum_{\omega=1}^5 \text{Re} \left\{ \frac{\tilde{M}_{5\omega} \tilde{N}_{\omega N} p_\omega}{\sqrt{\cos \hat{\theta} + p_\omega \sin \hat{\theta}}} \right\}, \\ q_2^N &= \sum_{\omega=1}^5 \text{Re} \left\{ \frac{\tilde{M}_{5\omega} \tilde{N}_{\omega N}}{\sqrt{\cos \hat{\theta} + p_\omega \sin \hat{\theta}}} \right\}\end{aligned}\quad (11)$$

$$\begin{aligned} d_i^N &= \sum_{\varpi=1}^5 \operatorname{Re} \left\{ \tilde{A}_{i\varpi} \tilde{N}_{\varpi N} \sqrt{\cos \hat{\theta} + p_{\varpi} \sin \hat{\theta}} \right\}, \\ v^N &= \sum_{\varpi=1}^5 \operatorname{Re} \left\{ \tilde{A}_{4\varpi} \tilde{N}_{\varpi N} \sqrt{\cos \hat{\theta} + p_{\varpi} \sin \hat{\theta}} \right\}; \\ w^N &= \sum_{\varpi=1}^5 \operatorname{Re} \left\{ \tilde{A}_{5\varpi} \tilde{N}_{\varpi N} \sqrt{\cos \hat{\theta} + p_{\varpi} \sin \hat{\theta}} \right\} \end{aligned} \quad (12)$$

where $\operatorname{Re}\{\cdot\}$ represents the real part of the quantities in brackets. In Eq. (11), the denominator could always be determined since p_{ϖ} are the non-zero complex roots which are derived from equations of material constants. Notice also that there is no possibility of $\hat{\theta}$ for which both $\cos \hat{\theta}$ and $\sin \hat{\theta}$ are equal to zero. Moreover, $\cos \hat{\theta}$ is real and $p_{\varpi} \sin \hat{\theta}$ is a complex root with non-zero imaginary (Bui and Zhang, 2013).

The five conjugate pairs of the eigenvalues p_{ϖ} and the (5×5) eigenvectors $\tilde{A}_{M\varpi}$ are obtained through the characteristic eigenvalue equation

$$[\tilde{\mathbf{G}} + \tilde{\mathbf{\Pi}} \tilde{\mathbf{p}} + \tilde{\mathbf{T}} \tilde{\mathbf{p}}^2] \tilde{\mathbf{A}} = \mathbf{0} \quad (13)$$

where

$$\begin{aligned} \tilde{\mathbf{G}} &= \begin{pmatrix} C_{i1k1} & e_{i11} & h_{i11} \\ e_{1k1} & -\kappa_{11} & -\beta_{11} \\ h_{1k1} & -\beta_{11} & -\gamma_{11} \end{pmatrix}; \\ \tilde{\mathbf{\Pi}} &= \begin{pmatrix} C_{i2k1} + C_{i1k2} & e_{i21} + e_{i12} & h_{i21} + h_{i12} \\ e_{2k1} + e_{1k2} & -\kappa_{12} - \kappa_{21} & -\beta_{12} - \beta_{21} \\ h_{2k1} + h_{1k2} & -\beta_{12} - \beta_{21} & -\gamma_{12} - \gamma_{21} \end{pmatrix}; \\ \tilde{\mathbf{T}} &= \begin{pmatrix} C_{i2k2} & e_{i22} & h_{i22} \\ e_{2k2} & -\kappa_{22} & -\beta_{22} \\ h_{2k2} & -\beta_{22} & -\gamma_{22} \end{pmatrix}; \quad \tilde{\mathbf{A}} = \begin{bmatrix} \tilde{A}_i \\ \tilde{A}_4 \\ \tilde{A}_5 \end{bmatrix} \end{aligned} \quad (14)$$

Only the five eigenvalues p_{ϖ} having positive imaginary part and their corresponding eigenvectors are utilized in the analysis. Finally, the (5×5) matrix $\tilde{M}_{M\varpi}$ can thus be determined by Rao and Kuna (2008) and Yu et al. (2014)

$$\tilde{M}_{M\varpi} = \begin{bmatrix} (C_{i2k1} + C_{i2k2} p_{\varpi}) \tilde{A}_{k\varpi} & (e_{1i2} + e_{2i2} p_{\varpi}) \tilde{A}_{4\varpi} \\ (e_{2k1} + e_{2k2} p_{\varpi}) \tilde{A}_{k\varpi} & (-\kappa_{21} - \kappa_{22} p_{\varpi}) \tilde{A}_{4\varpi} \\ (h_{2k1} + h_{2k2} p_{\varpi}) \tilde{A}_{k\varpi} & (-\beta_{21} - \beta_{22} p_{\varpi}) \tilde{A}_{4\varpi} \end{bmatrix}$$

with $\tilde{N}_{\varpi N} = [\tilde{M}_{M\varpi}]^{-1}$.

3. Dynamic XIGA formulation for fractures in magnetoelectroelasticity

The major source giving rise to the difficulties in fracture simulation of multiphase MEE composites lies in the inherent electro-magneto-mechanical coupling effect and the anisotropic behaviors of materials. Numerical methods based on the NURBS basis functions are ideally suitable for problems with smooth solutions due to their high-order continuity. On the other hand, for problems with non-smooth solutions like cracks, a local partition of unity (PU) enrichment method turns to be more appropriate. For

that reason, we are going to present in this section a numerical approach that incorporates the enrichment method with the NURBS-based IGA to model the cracks in MEE composites.

3.1. Brief on the NURBS basis functions

For self-contained reason or the sake of completeness, a brief on the NURBS basis function is thus presented. However, a comprehensive description of the NURBS basis functions and other numerical and mathematical aspects concerning with the theory of NURBS can be found in Piegl and Tiller (1995). Basically, a knot vector Ξ in a 1D parametric space $\xi \in [0, 1]$ to construct the B-spline basis functions is a set of non-decreasing real numbers, called knots, i.e.,

$$\Xi = \{\xi_1 = 0, \dots, \xi_{n+p+1} = 1\} \text{ with } \xi_i \in \mathbb{R} \text{ and } \xi_i \leq \xi_{i+1} \quad (16)$$

In Eq. (16), ξ_i , n and p denote a knot, the number of univariate spline basis functions defined on the knot vector, and the polynomial order of basis functions, respectively. The non-zero characteristic interval $[\xi_i, \xi_{i+1})$ is termed as knot span (or element) in IGA. An open knot vector Ξ is defined once the two ends of the knot are repeated $p+1$ times.

$$\Xi = \{\xi_1 = \dots, \xi_{p+1} = 0, \xi_{p+2}, \dots, \xi_n, \xi_{n+1} = \dots, \xi_{n+p+1} = 1\} \quad (17)$$

Given a knot vector Ξ , the B-spline basis functions of degree p , $N_{i,p}(\xi)$, using the Cox-de Boor recursion formula are defined as (Cottrell et al., 2009; Yu et al., 2015; Yin et al., 2014; Yin et al., 2015; Yin et al., 2015; Shojaee et al., 2012; Valizadeh et al., 2013; Valizadeh et al., 2013; Nguyen et al., 2014; Yu et al., 2014)

$$N_{i,0}(\xi) = \begin{cases} 1 & \xi_i \leq \xi < \xi_{i+1} \\ 0 & \text{otherwise} \end{cases}; \quad \text{for } p = 0 \quad (18)$$

$$\begin{bmatrix} (h_{1i2} + h_{2i2} p_{\varpi}) \tilde{A}_{5\varpi} \\ (-\beta_{21} - \beta_{22} p_{\varpi}) \tilde{A}_{5\varpi} \\ (-\gamma_{21} - \gamma_{22} p_{\varpi}) \tilde{A}_{5\varpi} \end{bmatrix} \quad (15)$$

$$\begin{aligned} N_{i,p}(\xi) &= \frac{\xi - \xi_i}{\xi_{i+p} - \xi_i} N_{i,p-1}(\xi) \\ &+ \frac{\xi_{i+p+1} - \xi}{\xi_{i+p+1} - \xi_{i+1}} N_{i+1,p-1}(\xi); \quad \text{for } p \geq 1 \end{aligned} \quad (19)$$

Unlike the FEM where the Lagrange polynomials are explicit functions, the IGA basis functions are on the parametric form as shown in Eqs. (18) and (19). Once the basis functions are evaluated, the ratios of the form 0/0 are set to be zeros.

The NURBS, $R_i^p(\xi)$, constructed by a weighted average of the B-spline basis functions are given by

$$R_i^p(\xi) = \frac{N_{i,p}(\xi)w_i}{W(\xi)} = \frac{N_{i,p}(\xi)w_i}{\sum_{j=1}^n N_{j,p}(\xi)w_j} \quad (20)$$

where $W(\xi) = \sum_{j=1}^n N_{j,p}(\xi)w_j$, with w_i being the i th weight. The NURBS basis function is degenerated into B-spline basis function for $w_i = 1$. Similarly, the bivariate NURBS basis functions are expressed as

$$\begin{aligned} R_{i,j}^{p,q}(\xi, \eta) &= \frac{N_{i,p}(\xi)M_{j,q}(\eta)w_{i,j}}{W(\xi, \eta)} \\ &= \frac{N_{i,p}(\xi)M_{j,q}(\eta)w_{i,j}}{\sum_{s=1}^n \sum_{t=1}^m N_{s,p}(\xi)M_{t,q}(\eta)w_{s,t}} \end{aligned} \quad (21)$$

where $w_{i,j}$ are the 2D weight; $N_{i,p}(\xi)$ and $M_{j,q}(\eta)$ are the B-spline basis functions defined on the two knot vectors $\Xi(\xi)$ and $\Xi(\eta)$, respectively, followed the recursive formula in Eqs. (18) and (19). In Eq. (19), $W(\xi, \eta)$ is defined as

$$W(\xi, \eta) = \sum_{s=1}^n \sum_{t=1}^m N_{s,p}(\xi)M_{t,q}(\eta)w_{s,t} \quad (22)$$

So, when the NURBS basis functions are determined, a NURBS curve is then constructed from linear combination of NURBS basis functions as

$$\mathbf{C}(\xi) = \sum_{i=1}^n R_i^p(\xi) \mathbf{P}_i \quad (23)$$

and also, a NURBS surface of orders p, q in the ξ, η directions can then formed by

$$\mathbf{S}(\xi, \eta) = \sum_{i=1}^n \sum_{j=1}^m R_{i,j}^{p,q}(\xi, \eta) \mathbf{P}_{i,j} \quad (24)$$

In Eqs. (23) and (24), \mathbf{P}_i and $\mathbf{P}_{i,j}$ are the coordinates of $n \times m$ control points in 1D and 2D, respectively. The control points serve as the degree of freedom (DOFs) in IGA. The number of non-zero basis function for a specified knot span (or element) is determined by the polynomial degree in both directions, i.e., $(p+1) \times (q+1)$. The total numbers of control points per element are thus determined by $n_{iga} = (p+1) \times (q+1)$. One must be noted that the NURBS basis functions also form a partition of unity, implying that $\forall \xi, \sum_{i=1}^n R_{i,p}(\xi) = 1$. Furthermore, the support of $R_{i,p}(\xi)$ is compact and contained in interval $[\xi_i, \xi_{i+p+1}]$ (Yu et al., 2015; Yin et al., 2014; Yin et al., 2015; Yin et al., 2015; Shojaee et al., 2012; Valizadeh et al., 2013; Valizadeh et al., 2013; Nguyen et al., 2014).

For a better observation and understanding of the situation, an evident example of revealing B-spline basis functions for different orders, $p = 1, 2$ and 3 is schematically depicted in Fig. 1 in which the knot vector $\Xi = \{0, 0, .2, .2, .4, .6, .8, .8, 1, 1\}$ for $p = 1$; $\Xi = \{0, 0, 0, .2, .2, .4, .6, .8, .8, 1, 1, 1\}$ for $p = 2$ and $\Xi = \{0, 0, 0, 0, .2, .2, .2, .4, .6, .8, .8, .8, 1, 1, 1, 1\}$ for $p = 3$ are employed. It is worth noting that the basis function of $p = 1$ corresponds to the linear shape functions in FEA, and the $p = 2$ and $p = 3$ basis functions resemble the shape functions of quadratic and cubic elements of FEA.

3.2. Enriched isogeometric approximation

Similar to XFEM, the discontinuity and singularity induced by the crack in XIGA are modeled by adding

appropriate enrichment functions to the conventional finite element function spaces. However, the additional degrees of freedom (DOFs) in XIGA are performed on the control points affected by the cracks. More precisely, the control points at the crack tips are enriched by asymptotic crack-tip enrichment functions whereas those at the crack faces are enriched by Heaviside functions. The geometric representation without cracks in the physical coordinates $\mathbf{X} = (x, y)$ based on the NURBS basis functions associated with a set of control points is expressed as (Cottrell et al., 2009; Benson et al., 2010; De Luycker et al., 2011; Yu et al., 2016c; Ghorashi et al., 2011; Bui, 2015; Yu et al., 2016b; Bhardwaj et al., 2015; Ghorashi et al., 2015; Bhardwaj et al., 2015)

$$\mathbf{X}(\xi) = \sum_{I=1}^{n_{iga}} R_I(\xi) \mathbf{P}_I \quad (25)$$

where $R_I(\xi)$ are the NURBS basis functions at the control point I .

At a particular point $\xi = (\xi, \eta)$ in parameter coordinates, the enriched approximation field can be expressed in general form as

$$\mathbf{u}(\xi) = \underbrace{\sum_{I=1}^{n_{iga}} R_I(\xi) \mathbf{u}_I}_{\text{standard}} + \text{enrichment} \quad (26)$$

where \mathbf{u}_I are the nodal parameters at the control point I . By employing the appropriate enrichment terms in Eq. (26), the enriched IGA approximation is constructed and can be used to capture the crack precisely.

Unlike the constituent materials, the primary variables for multiphase MEE composites involve not only the mechanical displacements u_i , but also the electric potential ϕ , and the magnetic potential φ . The enriched isogeometric approximations being considered in this work is extrinsic and local. By introducing the modified Heaviside and branch functions to Eq. (26), the enriched isogeometric approximations are given by

$$\begin{aligned} \{\mathbf{u}^h(\xi), \phi^h(\xi), \varphi^h(\xi)\} &= \sum_{I \in S} R_I(\xi) \{\mathbf{u}_I, \phi_I, \varphi_I\} \\ &+ \sum_{N_c=1}^{n_{cf}} \sum_{I \in S_c} R_I(\xi) [H(\xi) - H(\xi_I)] \{ \mathbf{a}_I, c_I, s_I \} \\ &+ \sum_{M_t=1}^{m_{ct}} \sum_{I \in S_t} R_I(\xi) \left\{ \sum_{k=1}^8 [F^k(\hat{r}, \hat{\theta}, \mu_k^{(re)}, \mu_k^{(im)}) \right. \\ &\quad \left. - F^k(\xi_I, \mu_k^{(re)}, \mu_k^{(im)})] \{ \mathbf{b}_I^k, d_I^k, t_I^k \} \right\} \end{aligned} \quad (27)$$

where ϕ_I and φ_I represent the vectors of the DOFs containing the electric potential and magnetic potential at control points. $\mu_k^{(re)}$ and $\mu_k^{(im)}$ are the real and imaginary parts of a complex number μ_k , respectively. S is the set of all nodes, S_c is the set of nodes for the physical elements that are completely cut by the crack (see Fig. 2), while S_t is the set of nodes around the crack tip (see Fig. 2). The additional DOFs associated with the crack-faces and crack-tip are represented by \mathbf{a}_I, c_I, s_I and $\mathbf{b}_I^k, d_I^k, t_I^k$, respectively. n_{cf}

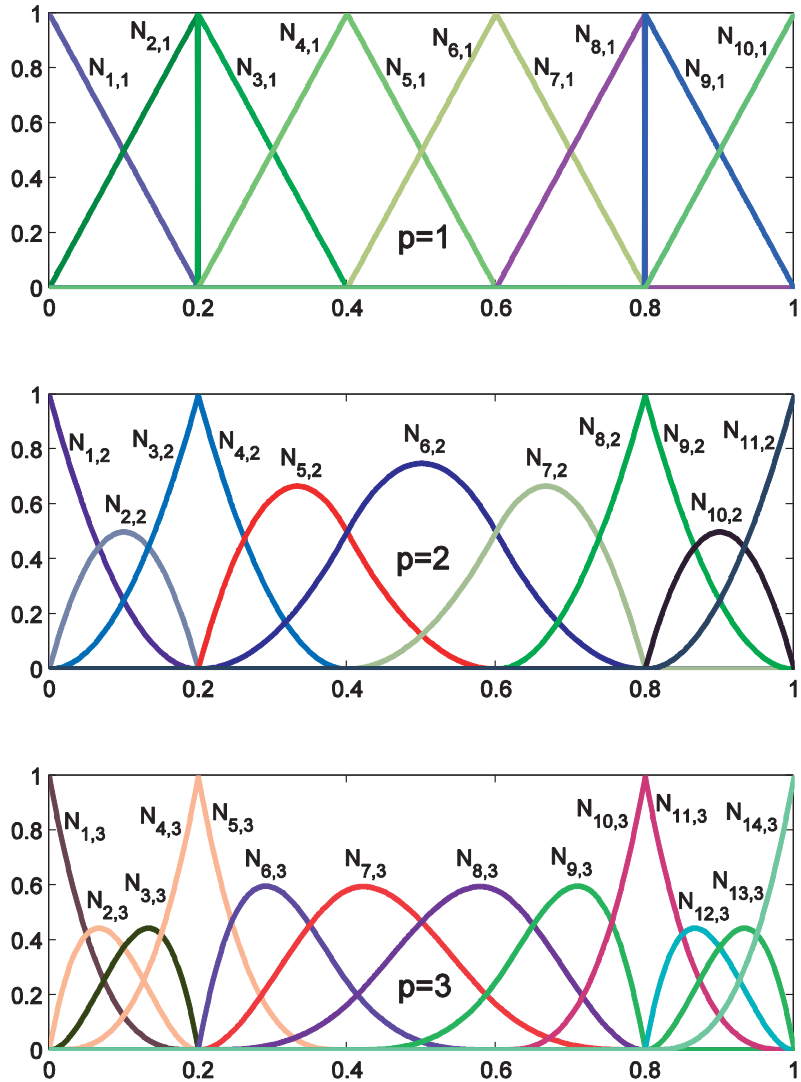


Fig. 1. Schematic representation of B-spline basis functions for an open non-uniform knot vector: $\Xi = \{0, 0, 0.2, 0.2, 0.4, 0.4, 0.6, 0.6, 0.8, 0.8, 1, 1\}$ ($p = 1$); $\Xi = \{0, 0, 0, 0.2, 0.2, 0.4, 0.4, 0.6, 0.6, 0.8, 0.8, 1, 1, 1\}$ ($p = 2$); and $\Xi = \{0, 0, 0, 0, 0.2, 0.2, 0.4, 0.4, 0.6, 0.6, 0.8, 0.8, 0.8, 0.8, 1, 1, 1, 1\}$ ($p = 3$).

defines the number of basis functions whose support is fully intersected by the crack-face, excluding the crack-tip (Bhardwaj et al., 2015), and this is identically the control points set enriched by the discontinuous Heaviside functions $H(\xi)$, which is the associated enrichment function for discontinuity N_c . In a similar manner, m_{ct} defines the number of basis functions whose support is partially intersected by the crack-tip, and this is the control points set enriched by the eightfold electro-magneto-mechanical branch functions F^k , which is the associated enrichment function for singularity M_t , and will be explained later in detail.

In Eq. (27), $H(\xi)$ denotes the discontinuous Heaviside function, which takes -1 or $+1$ depending on the current location of the parameter coordinates ξ over the crack-face. At a certain integration point in element, $H(\xi)$ takes -1 if the parameter coordinates ξ corresponding to that integration point lies below the crack-face, otherwise it takes $+1$. In the numerical simulation this implies that $H(\xi_i)$ takes

-1 and $+1$ depending on the location of the considered control point that locates below and above the crack face (Bhardwaj et al., 2015).

The present enriched isogeometric approximations are schematically illustrated in Fig. 2 for a central crack representing the physical mesh, control points, crack-face enriched control points, crack-tip enriched control points, and so on using a cubic (degree 3) NURBS basis function, respectively. In XIGA, it must be noted that the order of the NURBS basis functions alters the enrichment domain (Bhardwaj et al., 2015). Basically, the higher order of the basis functions is taken, the larger influence domains of the enrichment function are obtained. We will address this issue again in the numerical examples.

3.3. Branch functions for multiphase magnetoelasticity

Unlike the simple form of branch functions used for non-polarized isotropic solids, the branch enrichment

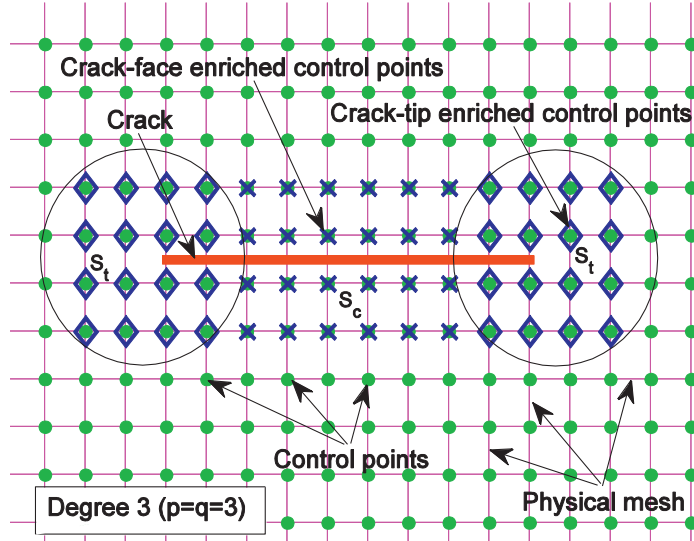


Fig. 2. Representation of physical mesh, control points, crack tip enriched control points, and crack face enriched control points for a crack discretized by the XIGA using a cubic (degree 3) NURBS net. The blue cross sign represents the control points enriched by Heaviside functions; while the blue diamond sign represents the control points enriched by the asymptotic crack tip branch functions. S_c defines the set of nodes for the physical elements that are completely cut by the crack and S_t denotes the set of nodes around the crack tip. (For interpretation of the references to color in this figure legend, the reader is referred to the web version of this article.)

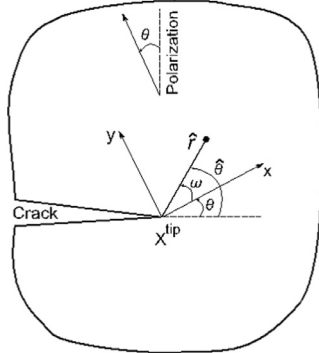


Fig. 3. Notation of the material axes at the crack tip and its polarization in a domain.

functions for polarized materials like magnetoelectroelastic under consideration however are much more complicated. They are one of the most challenging tasks when dealing with fracture in polarized materials in terms of discrete approaches like the developed method. In Eq. (27), the terms $F^k(\hat{r}, \hat{\theta}, \mu_k^{(re)}, \mu_k^{(im)})$ are the asymptotic crack-tip enrichment functions. The eightfold branch functions $F^k(\hat{r}, \hat{\theta}, \mu_k^{(re)}, \mu_k^{(im)})$ particularly suitable for the multiphase piezoelectric/piezomagnetic materials are proposed in Rojas-Diaz et al. (2011) which consider the effect of electro-magneto-mechanical properties. They are given by

$$F^k(\hat{r}, \hat{\theta}, \mu_k^{(re)}, \mu_k^{(im)}) = \sqrt{\hat{r}} \{g_1(\hat{\theta}), g_2(\hat{\theta}), g_3(\hat{\theta}), g_4(\hat{\theta}), \\ g_5(\hat{\theta}), g_6(\hat{\theta}), g_7(\hat{\theta}), g_8(\hat{\theta})\} \quad (28)$$

As sketched in Fig. 3, arbitrary poling directions can be accessible by introducing an angle $\omega = \hat{\theta} - \theta$, where θ de-

fines the orientation of the material axes versus the crack line. The functions $g_{\hat{m}}(\hat{\theta})$ are hence determined by the following condition (Bui and Zhang, 2013; Rojas-Diaz et al., 2011)

$$g_{\hat{m}}(\hat{\theta}) = \begin{cases} \rho_{\hat{m}}(\omega(\theta, \hat{\theta}), \mu_{\hat{m}}^{(re)}, \mu_{\hat{m}}^{(im)}) & \text{if } \mu_{\hat{m}}^{(im)} > 0 \\ \cos\left(\frac{\psi_{\hat{m}}(\omega(\theta, \hat{\theta}), \mu_{\hat{m}}^{(re)}, \mu_{\hat{m}}^{(im)})}{2}\right) & \text{if } \mu_{\hat{m}}^{(im)} \leq 0 \\ \rho_{\hat{m}}(\omega(\theta, \hat{\theta}), \mu_{\hat{m}}^{(re)}, \mu_{\hat{m}}^{(im)}) & \\ \sin\left(\frac{\psi_{\hat{m}}(\omega(\theta, \hat{\theta}), \mu_{\hat{m}}^{(re)}, \mu_{\hat{m}}^{(im)})}{2}\right) & \end{cases} \quad (29)$$

The complex numbers $\mu_{\hat{m}} = \mu_{\hat{m}}^{(re)} + i\mu_{\hat{m}}^{(im)}$, with $i = \sqrt{-1}$ being the imaginary unit, are the eight roots of the following characteristic equation:

$$[a_{11}\mu^4 + (2a_{12} + a_{33})\mu^2 + a_{22}] \\ \times [(\Delta_{11}\mu^2 + \Delta_{22})^2 - (\delta_{11}\mu^2 + \delta_{22})(\zeta_{11}\mu^2 + \zeta_{22})] \\ - [(b_{21} + b_{13})\mu^2 + b_{22}]^2(\zeta_{11}\mu^2 + \zeta_{22}) \\ - [(d_{21} + d_{13})\mu^2 + d_{22}]^2(\delta_{11}\mu^2 + \delta_{22}) \\ + 2[(b_{21} + b_{13})\mu^2 + b_{22}][(d_{21} + d_{13})\mu^2] \\ \times (\Delta_{11}\mu^2 + \Delta_{22}) = 0 \quad (30)$$

in which the coefficients a_{ij} , b_{ij} , δ_{ij} , Δ_{ij} and ζ_{ij} represent the reduced material constants, and detail information can be found in Rojas-Diaz et al. (2011). In general, the roots of Eq. (30) are complex with four conjugate pairs such as $\mu_1 = \alpha_1 + i\beta_1$, $\mu_2 = \alpha_2 + i\beta_2$; $\mu_3 = \alpha_3 + i\beta_3$; $\mu_4 = \alpha_4 + i\beta_4$; $\mu_5 = \bar{\mu}_1$; $\mu_6 = \bar{\mu}_2$; $\mu_7 = \bar{\mu}_3$ and $\mu_8 = \bar{\mu}_4$. In Eq. (29), the modified angle $\psi_{\hat{m}}(\omega(\theta, \hat{\theta}), \mu_{\hat{m}}^{(re)}, \mu_{\hat{m}}^{(im)})$ is

determined by

$$\begin{aligned} \psi_{\hat{m}}(\omega(\theta, \hat{\theta}), \mu_{\hat{m}}^{(re)}, \mu_{\hat{m}}^{(im)}) &= \frac{\pi}{2} + \pi \operatorname{int}\left(\frac{\omega}{\pi}\right) \\ &- \arctan\left(\frac{\cos\left(\theta - \pi \operatorname{int}\left(\frac{\omega}{\pi}\right)\right) + \mu_{\hat{m}}^{(re)} \sin\left(\omega(\theta, \hat{\theta}) - \pi \operatorname{int}\left(\frac{\omega}{\pi}\right)\right)}{\left|\mu_{\hat{m}}^{(im)}\right| \sin\left(\omega - \pi \operatorname{int}\left(\frac{\omega}{\pi}\right)\right)}\right) \end{aligned} \quad (31)$$

and the modified radius $\rho_{\hat{m}}(\omega(\theta, \hat{\theta}), \mu_{\hat{m}}^{(re)}, \mu_{\hat{m}}^{(im)})$ is also estimated through the following expression

$$\begin{aligned} \rho_{\hat{m}}(\omega(\theta, \hat{\theta}), \mu_{\hat{m}}^{(re)}, \mu_{\hat{m}}^{(im)}) &= \frac{1}{\sqrt{2}} \\ &\times \sqrt[4]{(\mu_{\hat{m}}^{re})^2 + (\mu_{\hat{m}}^{im})^2 + \mu_{\hat{m}}^{(re)} \sin(2\omega) - ((\mu_{\hat{m}}^{re})^2 + (\mu_{\hat{m}}^{im})^2 - 1) \cos(2\omega)} \end{aligned} \quad (32)$$

It is important to note that the eightfold electro-magneto-mechanical branch functions derived in Eq. (28) are to attain a full description of the electro-magneto-mechanical crack tip solutions in MEE materials in which the electric and magnetic fields are completely described. The poling variation of material directions at the crack face can thus be made accordingly.

The fourfold pure mechanical enrichment functions used for isotropic materials found previously can be utilized for multiphase MEE materials with a slight difference on the results as compared with the complex eightfold electro-magneto-mechanical ones in a similar setting. This fact and the reason may be due to the weak magnitude of the coupling effect among the mechanical, electric and magnetic fields in MEE materials. The fourfold mechanical branch functions (Fleming et al., 1997)

$$\begin{aligned} F^k(\hat{r}, \hat{\theta}) &= \sqrt{\hat{r}} \left\{ \sin\left(\frac{\hat{\theta}}{2}\right), \cos\left(\frac{\hat{\theta}}{2}\right), \sin\left(\frac{\hat{\theta}}{2}\right) \sin(\hat{\theta}), \right. \\ &\quad \left. \cos\left(\frac{\hat{\theta}}{2}\right) \sin(\hat{\theta}) \right\} \end{aligned} \quad (33)$$

are hence considered in this work just to show its applicability in dynamic impact problems.

A very important issue to be noted is that the eightfold branch functions defined for MEE materials depend on the material constants, polarization angle and volume fraction, but do not depend on the applied loads. Even in the absence of the electric and magnetic loadings, one can obtain the non-zero stress fields, electric displacement and magnetic induction by using constitutive equations or due to the electric-magnetic-mechanical effect. More importantly, the eightfold branch functions defined for MEE materials in Eq. (28) will not be degenerated to the fourfold pure mechanical basis functions in Eq. (33) even in the absence of the electric and magnetic fields.

3.4. Weak-form and discrete equations

The governing equations for the coupled magneto-electro-mechanical initial-boundary value problem are

given in weak form through the introduction of the weighting quantities $\delta\mathbf{u}$ – virtual displacements, $\delta\phi$ – virtual electric potential, and $\delta\varphi$ – virtual magnetic potential (Bui and Zhang, 2013)

$$\begin{aligned} \int_{\Omega} \rho \delta\mathbf{u}^T \ddot{\mathbf{u}} d\Omega + \int_{\Omega} \delta\mathbf{e}^T \sigma d\Omega \\ - \int_{\Omega} \delta\mathbf{u}^T \mathbf{f}_{\text{mech}} d\Omega - \int_{\Gamma_B} \delta\mathbf{u}^T \bar{\mathbf{t}}^{\text{mech}} d\Gamma = 0 \\ \int_{\Omega} \delta\mathbf{E}^T \mathbf{D} d\Omega - \int_{\Omega} \delta\phi f^{\text{elec}} d\Omega - \int_{\Gamma_D} \delta\phi \bar{t}^{\text{elec}} d\Gamma = 0 \\ \int_{\Omega} \delta\mathbf{H}^T \mathbf{B} d\Omega - \int_{\Omega} \delta\varphi f^{\text{mag}} d\Omega - \int_{\Gamma_B} \delta\varphi \bar{t}^{\text{mag}} d\Gamma = 0 \end{aligned} \quad (34)$$

The discrete dynamic XIGA equations for a system without damping effect can hence be obtained by substituting the given enriched approximation functions in Eq. (27) into the weak form Eq. (34):

$$\mathbf{M}\ddot{\mathbf{d}} + \mathbf{K}\mathbf{d} = \mathbf{F} \quad (35)$$

where \mathbf{M} , \mathbf{K} and \mathbf{d} are the global mass and stiffness matrices and the global unknown control variable vector of the system.

$$\mathbf{M} = \begin{bmatrix} \mathbf{M}_{mm} & \mathbf{0} & \mathbf{0} \\ \mathbf{0} & \mathbf{0} & \mathbf{0} \\ \mathbf{0} & \mathbf{0} & \mathbf{0} \end{bmatrix}; \quad \mathbf{K} = \begin{bmatrix} \mathbf{K}_{mm} & \mathbf{K}_{me} & \mathbf{K}_{m\bar{m}} \\ \mathbf{K}_{em} & \mathbf{K}_{ee} & \mathbf{K}_{e\bar{m}} \\ \mathbf{K}_{\bar{m}m} & \mathbf{K}_{\bar{m}e} & \mathbf{K}_{\bar{m}\bar{m}} \end{bmatrix} \quad (36)$$

in which the subscripts m , e , and \bar{m} represent the *mechanic*, *electric* and *magnetic* fields, respectively.

For the enriched elements, the elementary stiffness matrix (superscript [e]) is obtained as

$$\mathbf{K}_{ij}^{[e]} = \begin{bmatrix} \mathbf{K}_{ij}^{uu} & \mathbf{K}_{ij}^{u\alpha} & \mathbf{K}_{ij}^{u\beta} \\ \mathbf{K}_{ij}^{\alpha u} & \mathbf{K}_{ij}^{\alpha\alpha} & \mathbf{K}_{ij}^{\alpha\beta} \\ \mathbf{K}_{ij}^{\beta u} & \mathbf{K}_{ij}^{\beta\alpha} & \mathbf{K}_{ij}^{\beta\beta} \end{bmatrix}; \quad i, j = m, e, \bar{m} \quad (37)$$

whereas for the non-enriched elements

$$\mathbf{K}_{ij}^{[e]} = \mathbf{K}_{ij}^{uu} \quad (38)$$

In the above equations, we have denoted by $u = \{\mathbf{u}\varphi\}^T$, $\alpha = \{\mathbf{a}_I c_I\}^T$, $\beta = \{\mathbf{b}_I^k d_I^k t_I^k\}^T$, and the stiffness matrices are

$$\begin{aligned} \mathbf{K}_{ij}^{rs} &= \int_{\Omega^{[e]}} (\mathbf{B}_I^r)^T \bar{\mathbf{C}} (\mathbf{B}_J^s) d\Omega; r, s \cong u, \alpha, \beta \quad \text{and} \\ i, j &= m, e, \bar{m} \end{aligned} \quad (39)$$

and their components are detailed in Appendix A. In Eq. (39), $\bar{\mathbf{C}}$ is the generalized elasticity matrix of MEE material and

$$\mathbf{B}_I^u = \begin{bmatrix} R_{I,x} & 0 & 0 & 0 \\ 0 & R_{I,y} & 0 & 0 \\ R_{I,y} & R_{I,x} & 0 & 0 \\ 0 & 0 & R_{I,x} & 0 \\ 0 & 0 & R_{I,y} & 0 \\ 0 & 0 & 0 & R_{I,x} \\ 0 & 0 & 0 & R_{I,y} \end{bmatrix} \quad (40)$$

$$\mathbf{B}_I^\alpha = \begin{bmatrix} (R_I(H(\xi)) - H(\xi_I)),_x & 0 & 0 & 0 \\ 0 & (R_I(H(\xi)) - H(\xi_I)),_y & 0 & 0 \\ (R_I(H(\xi)) - H(\xi_I)),_y & (R_I(H(\xi)) - H(\xi_I)),_x & 0 & 0 \\ 0 & 0 & (R_I(H(\xi)) - H(\xi_I)),_x & 0 \\ 0 & 0 & (R_I(H(\xi)) - H(\xi_I)),_y & 0 \\ 0 & 0 & 0 & (R_I(H(\xi)) - H(\xi_I)),_x \\ 0 & 0 & 0 & (R_I(H(\xi)) - H(\xi_I)),_y \end{bmatrix} \quad (41)$$

$$\mathbf{B}_I^\beta = [\mathbf{B}_I^{\beta 1} \mathbf{B}_I^{\beta 2} \mathbf{B}_I^{\beta 3} \mathbf{B}_I^{\beta 4} \mathbf{B}_I^{\beta 5} \mathbf{B}_I^{\beta 6} \mathbf{B}_I^{\beta 7} \mathbf{B}_I^{\beta 8}] \quad (42)$$

$$\mathbf{B}_I^{\beta k} = \begin{bmatrix} \tilde{S}_x & 0 & 0 & 0 \\ 0 & \tilde{S}_y & 0 & 0 \\ \tilde{S}_y & \tilde{S}_x & 0 & 0 \\ 0 & 0 & \tilde{S}_x & 0 \\ 0 & 0 & \tilde{S}_y & 0 \\ 0 & 0 & 0 & \tilde{S}_x \\ 0 & 0 & 0 & \tilde{S}_y \end{bmatrix}$$

$$\begin{aligned} \tilde{S}_x &= (R_I(F^k(\hat{r}, \hat{\theta}, \mu_k^{(re)}, \mu_k^{(im)})) - F^k(\xi_I, \mu_k^{(re)}, \mu_k^{(im)})),_x \\ \tilde{S}_y &= (R_I(F^k(\hat{r}, \hat{\theta}, \mu_k^{(re)}, \mu_k^{(im)})) - F^k(\xi_I, \mu_k^{(re)}, \mu_k^{(im)})),_y \end{aligned} \quad (43)$$

Similarly, the elementary consistent mass matrix (supercript [e]) for enriched elements is obtained as

$$\mathbf{M}_{mm}^{[e]} = \begin{bmatrix} \mathbf{M}_{mm}^{uu} & \mathbf{M}_{mm}^{u\alpha} & \mathbf{M}_{mm}^{u\beta} \\ \mathbf{M}_{mm}^{\alpha u} & \mathbf{M}_{mm}^{\alpha\alpha} & \mathbf{M}_{mm}^{\alpha\beta} \\ \mathbf{M}_{mm}^{\beta u} & \mathbf{M}_{mm}^{\beta\alpha} & \mathbf{M}_{mm}^{\beta\beta} \end{bmatrix} \quad (44)$$

with $u = \{\mathbf{u}\phi\varphi\}^T$, $\alpha = \{\mathbf{a}_I c_I s_I\}^T$, $\beta = \{\mathbf{b}_I^k d_I^k t_I^k\}^T$, whereas for the non-enriched elements

$$\mathbf{M}_{mm}^{[e]} = \mathbf{M}_{mm}^{uu} \quad (45)$$

and their detailed components as

$$\begin{aligned} \mathbf{M}_{mm}^{uu} &= \int_{\Omega^{[e]}} \rho R_I^T R_I d\Omega; \\ \mathbf{M}_{mm}^{\alpha\alpha} &= \int_{\Omega^{[e]}} \rho (R_I(H(\xi)) - H(\xi_I))^T (R_J(H(\xi)) - H(\xi_J)) d\Omega; \\ \mathbf{M}_{mm}^{\beta\beta} &= \int_{\Omega^{[e]}} \rho \left(R_I(F^k(\hat{r}, \hat{\theta}, \mu_k^{(re)}, \mu_k^{(im)})) - (F^k(\xi_I, \mu_k^{(re)}, \mu_k^{(im)})) \right)^T \\ &\quad \left(R_J(F^k(\hat{r}, \hat{\theta}, \mu_k^{(re)}, \mu_k^{(im)})) - (F^k(\xi_J, \mu_k^{(re)}, \mu_k^{(im)})) \right) d\Omega; \\ \mathbf{M}_{mm}^{u\alpha} &= \mathbf{M}_{mm}^{\alpha u} = \int_{\Omega^{[e]}} \rho (R_I)^T (R_J(H(\xi)) - H(\xi_J)) d\Omega; \\ \mathbf{M}_{mm}^{u\beta} &= \mathbf{M}_{mm}^{\beta u} \\ &= \int_{\Omega^{[e]}} \rho (R_I)^T (R_J(F^k(\hat{r}, \hat{\theta}, \mu_k^{(re)}, \mu_k^{(im)})) - (F^k(\xi_J, \mu_k^{(re)}, \mu_k^{(im)}))) d\Omega; \\ \mathbf{M}_{mm}^{\alpha\beta} &= \mathbf{M}_{mm}^{\beta\alpha} = \int_{\Omega^{[e]}} \rho (R_I(H(\xi)) - H(\xi_I))^T \\ &\quad \left(R_J(F^k(\hat{r}, \hat{\theta}, \mu_k^{(re)}, \mu_k^{(im)})) - (F^k(\xi_J, \mu_k^{(re)}, \mu_k^{(im)})) \right) d\Omega \end{aligned} \quad (46)$$

In Eq. (35), \mathbf{F} represents the vector of the external control variable forces, and the element contribution to the global element force vector is given by

$$\mathbf{f}_I^{[e]} = \{\mathbf{f}_I^u \mathbf{f}_I^\alpha \mathbf{f}_I^{\beta 1} \mathbf{f}_I^{\beta 2} \mathbf{f}_I^{\beta 3} \mathbf{f}_I^{\beta 4} \mathbf{f}_I^{\beta 5} \mathbf{f}_I^{\beta 6} \mathbf{f}_I^{\beta 7} \mathbf{f}_I^{\beta 8}\}^T \quad (47)$$

for the enriched elements, whereas

$$\mathbf{f}_I^{[e]} = \mathbf{f}_I^u \quad (48)$$

for the non-enriched elements, in which

$$\mathbf{f}_I^u = \int_{\partial\Omega^{[e]}} R_I \bar{\mathbf{t}} d\Gamma + \int_{\Omega^{[e]}} R_I \bar{\mathbf{f}} d\Omega \quad (49)$$

$$\begin{aligned} \mathbf{f}_I^\alpha &= \int_{\partial\Omega^{[e]}} R_I (H(\xi) - H(\xi_I)) \bar{\mathbf{t}} d\Gamma \\ &\quad + \int_{\Omega^{[e]}} R_I (H(\xi) - H(\xi_I)) \bar{\mathbf{f}} d\Omega \end{aligned} \quad (50)$$

$$\begin{aligned} \mathbf{f}_I^{\beta k} &= \int_{\partial\Omega^{[e]}} R_I (F^k(\hat{r}, \hat{\theta}, \mu_k^{(re)}, \mu_k^{(im)})) \\ &\quad - F^k(\xi_I, \mu_k^{(re)}, \mu_k^{(im)}) \bar{\mathbf{t}} d\Gamma; \quad (k = 1, 8) \\ &\quad + \int_{\Omega^{[e]}} R_I (F^k(\hat{r}, \hat{\theta}, \mu_k^{(re)}, \mu_k^{(im)})) \\ &\quad - F^k(\xi_I, \mu_k^{(re)}, \mu_k^{(im)}) \bar{\mathbf{f}} d\Omega \end{aligned} \quad (51)$$

The derivative of the NURBS basis functions with respect to the physical coordinates in Eq. (40) can be calculated from (Ghorashi et al., 2011)

$$\begin{Bmatrix} \frac{\partial R_i}{\partial x} \\ \frac{\partial R_i}{\partial y} \end{Bmatrix} = \mathbf{J}^{-1} \begin{Bmatrix} \frac{\partial R_i}{\partial \xi} \\ \frac{\partial R_i}{\partial \eta} \end{Bmatrix} \quad (52)$$

in which the Jacobian matrix \mathbf{J} for the transformation between the parametric and physical spaces is determined as

$$\mathbf{J} = \begin{bmatrix} \frac{\partial x}{\partial \xi} & \frac{\partial y}{\partial \xi} \\ \frac{\partial x}{\partial \eta} & \frac{\partial y}{\partial \eta} \end{bmatrix} \quad (53)$$

3.5. Numerical integration and essential boundary conditions

The numerical integration with the Gaussian quadrature rule is adopted for the estimation of the stiffness, mass matrices and loading in the present formulation. Since the XIGA involves different types of elements in the systems including the crack face and crack tip elements with which the standard Gaussian quadrature rule can not be applied directly. Therefore, special techniques are required for precisely treating the numerical integration because of the existing the discontinuity and singularity induced by the cracks. In this paper, we adopt the triangular sub-domain

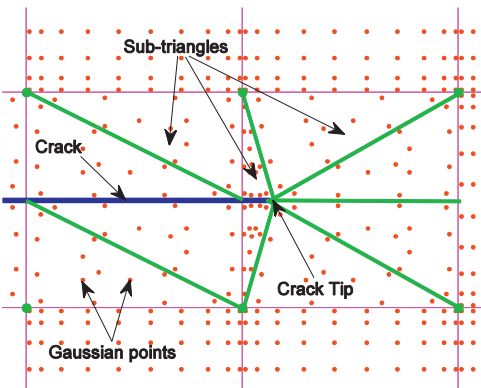


Fig. 4. Illustration of sub-triangulation for partitioning tip and cut elements of a crack in the framework of the XIGA setting.

technique (Dolbow, 1999; Ghorashi et al., 2011) as sketched in Fig. 4 for evaluating the numerical integration of the tip and cut elements. The distribution of integration points for different types of elements for a crack in terms of the XIGA setting is schematically depicted in Fig. 5 for $p = 1$ and $p = 2$. In this work, a high number of Gaussian points are applied to the cut and tip elements interested with the crack as well as neighbor elements around the crack tip to improve the accuracy of the results, while a lower order of the Gaussian points is employed for normal elements.

The accuracy of the numerical integration estimated over the cut and tip elements may be further improved if more sub-triangles are taken. However, the more sub-triangles may result in a very high cost of the computation. Alternatively, the accuracy may also be improved by, for instance, applying the so-called “almost polar integration” proposed by Laborde et al. (2005) for a better numerical integration of crack tip elements.

It is interesting to point out that the low-order IGA is identical to the FEM once the degree of NURBS is set to be unity. The Lagrange finite elements are identical to the first-order NURBS with uniform weights. So the low-order degree 1 XIGA with uniform weights degenerates to common XFEM.

Furthermore, as the NURBS basis functions generally do not satisfy the Kronecker delta function, special treatment methods for the enforcement of boundary conditions in IGA are thus required (Laborde et al., 2005). In this study, we adopt the direct imposition of the Dirichlet boundary condition. The Dirichlet-type boundary conditions of all the numerical examples, which will be examined in the numerical examples section, can be enforced by setting the corresponding control variables either to be zeros (the homogeneous BCs) or equal to the prescribed values (inhomogeneous BCs), assuming that the use of open knot vectors (Wang and Xuan, 2010; Hughes et al., 2005).

In this paper, the standard unconditionally stable implicit Newmark time integration scheme suitable for solving the discrete dynamic equilibrium equations of XIGA is used (Bui and Zhang, 2013; Bui and Zhang, 2012; Liu et al., 2013; Liu et al., 2014; Yu et al., 2015).

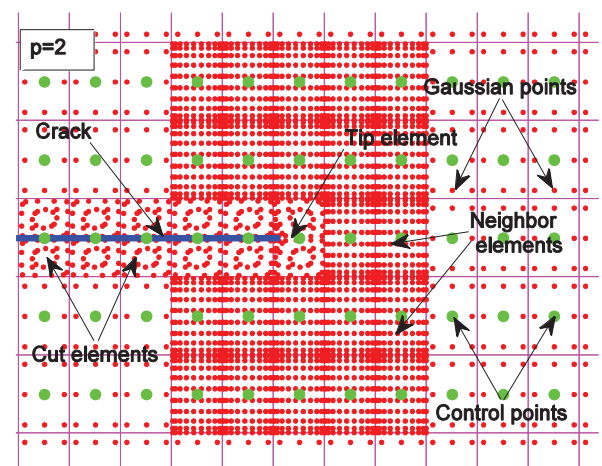
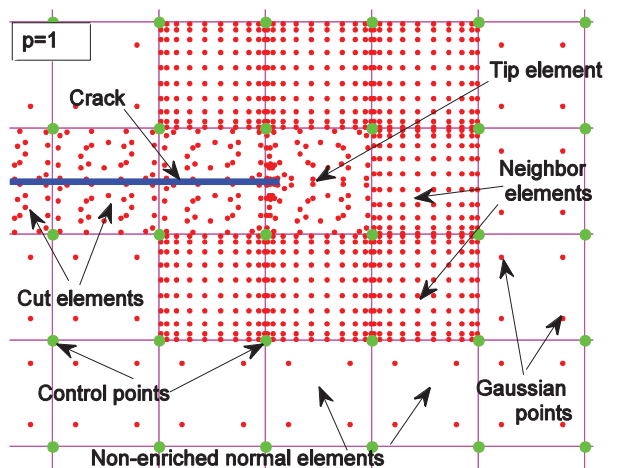


Fig. 5. Representation of integration point distributions for different elements of a crack in the XIGA setting ($p = 1$ and $p = 2$). A higher number of Gaussian points are used for the cut and tip elements as well as the neighbor elements to ensure not to lose the accuracy of the results. In this work, 4 integration points are used for non-enriched normal elements, 13 integration points for each sub-triangle element divided by cut and tip elements, while 10 integration points for the neighbor elements.

4. Computation of extended dynamic fracture parameters

The intensity factors are the crack tip characterizing parameters that reflect the strength of the singular field in linear elastic fracture mechanics. For multiphase MEE materials, the fracture parameters under dynamic loading and in 2D plane problems are thus characterized through the dynamic mechanical stress intensity factors (DSIF) K_{II} , K_I , the dynamic electrical displacement intensity factor (DEDIF) K_{IV} , and the dynamic magnetic induction intensity factor (DMIIF) K_V , which are determined in this study by using the electro-magneto-mechanical interaction integral, see Rao and Kuna (2008) and Bui and Zhang (2013) for more detail.

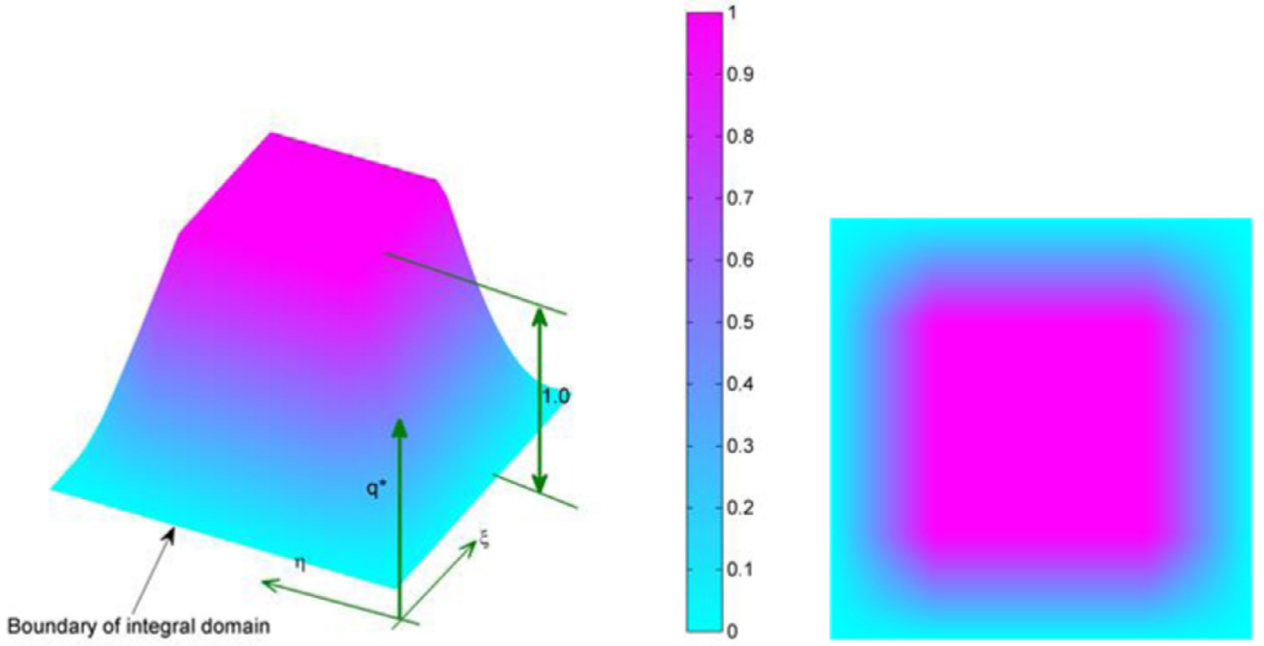


Fig. 6. Schematic representation of q^* smooth weight function used for the integral domain: front-view (left) and top-view (right).

$$\begin{aligned} I^{(1,2)} = & \int_A \left(\sigma_{ij}^{(1)} \frac{\partial u_i^{(2)}}{\partial x_1} + \sigma_{ij}^{(2)} \frac{\partial u_i^{(1)}}{\partial x_1} + D_j^{(1)} \frac{\partial \phi^{(2)}}{\partial x_1} \right. \\ & + D_j^{(2)} \frac{\partial \phi^{(1)}}{\partial x_1} + B_j^{(1)} \frac{\partial \varphi^{(2)}}{\partial x_1} + B_j^{(2)} \frac{\partial \varphi^{(1)}}{\partial x_1} - W^{(1,2)} \delta_{1j} \\ & \times \frac{\partial \tilde{q}}{\partial x_j} dA + \int_A \rho \left(\frac{\partial^2 u_i^{(1)}}{\partial t^2} \frac{\partial u_i^{(2)}}{\partial x_1} \right) q^* dA \end{aligned} \quad (54)$$

where the indices i and j vary from 1 to 2 in 2D MEE solid, δ_{1j} is the Kronecker delta property, q^* is an arbitrary smooth weight function chosen to be unity at the crack-tip and zero along the boundary of the domain A , and a smooth linear variation in-between, as sketched in Fig. 6. Here, A represents the area inside an arbitrary contour enclosing the crack tip (Rao and Kuna, 2008).

In Eq. (54), the electric enthalpy density $W^{(1,2)}$ for electro-magneto-mechanical loading for two states is determined by Rao and Kuna (2008)

$$W^{(1,2)} = \frac{1}{2} \left(\sigma_{ij}^{(1)} \varepsilon_{ij}^{(2)} + \sigma_{ij}^{(2)} \varepsilon_{ij}^{(1)} - D_j^{(1)} E_j^{(2)} \right. \\ \left. - D_j^{(2)} E_j^{(1)} - B_j^{(1)} H_j^{(2)} - B_j^{(2)} H_j^{(1)} \right) \quad (55)$$

It must be addressed here that Eq. (54) is valid only for a crack lying in x_1 -direction, and the superscripts (1) and (2) represent the two independent dynamic equilibrium states of a cracked body – the actual state under study and the auxiliary state selected as the asymptotic crack-tip fields of any fracture modes. The detail of the asymptotic crack-tip fields is given in Section 2.3 (Bui and Zhang, 2013; Rao and Kuna, 2008).

5. Numerical results and discussions

In this section, three representative numerical examples are studied to demonstrate the accuracy of the proposed

Table 1

Material properties of multiphase composite $\text{BaTiO}_3\text{-CoFe}_2\text{O}_4$ with volume fraction $v_f = 0.5$.

$$\begin{aligned} C_{11} &= 226.0 \text{ GPa}; C_{12} = 125.0 \text{ GPa}; C_{22} = 216.0 \text{ GPa}; C_{66} = 44.0 \text{ GPa}; \\ e_{21} &= -2.2 \text{ C/m}^2; e_{22} = 9.3 \text{ C/m}^2; e_{16} = 5.8 \text{ C/m}^2; \\ h_{21} &= 290.2 \text{ N/Am}; h_{22} = 350.0 \text{ N/Am}; h_{16} = 275.0 \text{ N/Am}; \\ \kappa_{11} &= 56.4 \times 10^{-10} \text{ C}^2/\text{Nm}^2; \kappa_{22} = 63.5 \times 10^{-10} \text{ C}^2/\text{Nm}^2; \\ \beta_{11} &= 5.367 \times 10^{-12} \text{ Ns/VC}; \beta_{22} = 2737.5 \times 10^{-12} \text{ Ns/VC}; \\ \gamma_{11} &= 297.0 \times 10^{-6} \text{ Ns}^2/\text{C}^2; \gamma_{22} = 83.5 \times 10^{-6} \text{ Ns}^2/\text{C}^2. \end{aligned}$$

XIGA for the transient dynamic fracture analysis of multiphase MEE materials. Dynamic responses of the extended intensity factors for cracked MEE plates obtained by the XIGA are examined and compared with the reference solutions from the time-domain BEM (Wünsche et al., 2012) and the dynamic XFEM (Bui and Zhang, 2013). In addition, the coupling magneto-electro-mechanical effect in the MEE composites is also investigated.

All numerical examples are considered to be under the plane strain situation, and the electrically and magnetically impermeable crack face boundary conditions are assumed. The fine physical meshes are used unless stated otherwise. The $\text{BaTiO}_3\text{-CoFe}_2\text{O}_4$ material, see Table 1 for its constants, with a volume fraction $v_f = 0.5$ is taken for the analysis (Wünsche et al., 2012; Bui and Zhang, 2013). If not specified otherwise a mass density of $\rho = 5500 \text{ kg/m}^3$ is used throughout the study.

In this paper, the weights taken for creating the NURBS basis functions are assumed to be unity and all knot vectors are open and uniform. A dynamic XIGA model having the order of the NURBS in parametric spaces in both directions are $p = q = 3$ is used and termed ‘Degree 3 XIGA’ for the abbreviation. The eightfold electro-magneto-mechanical branch functions are mainly used in the numerical study, but the standard fourfold mechanical enrichment functions are also tested in some particular cases.

For numerical integration, we adopt a 4×4 Gaussian quadrature for standard elements, sub-division triangle techniques with higher Gaussian quadrature – 13×13 per each sub-triangle for crack tip and cut elements, while a 10×10 quadrature order is used for the neighbor elements.

Furthermore, the polarization direction that we consider in all the numerical examples can be arbitrary. In what follows, the plates being studied are subjected either to:

- pure mechanical tensile impact load $\sigma_{22}(t) = \sigma_0 H(t)$,
- or pure impact electrical load $D_2(t) = D_0 H(t)$,
- or pure impact magnetic load $B_2(t) = B_0 H(t)$,
- or coupled electro-magneto-mechanical load $\sigma_{22}(t) = \sigma_0 H(t)$, $D_2(t) = D_0 H(t)$ and $B_2(t) = B_0 H(t)$

where the parameters σ_0 , D_0 and B_0 define the amplitudes of mechanical, electric and magnetic loadings, and $H(t)$ is the Heaviside step function (Wünsche et al., 2012; Rojas-Díaz et al., 2011; Bui and Zhang, 2013). All the numerical results are presented for the normalized extended dynamic intensity factors (NDIFs) against the dimensionless time $t^* = tc_L/h$, where $c_L = \sqrt{C_{22}/\rho}$ is the quasi-longitudinal wave velocity. The extended dynamic fracture parameters K_{II} , K_I , K_{IV} , and K_V are then normalized by the following formations for convince:

$$\begin{aligned} K_I^* &= \frac{K_I}{\sigma_0 \sqrt{\pi a}}; \quad K_{II}^* = \frac{K_{II}}{\sigma_0 \sqrt{\pi a}}; \quad K_{IV}^* = \frac{e_{22}}{\kappa_{22}} \frac{K_{IV}}{\sigma_0 \sqrt{\pi a}}; \\ K_V^* &= \frac{h_{22}}{\gamma_{22}} \frac{K_V}{\sigma_0 \sqrt{\pi a}} \end{aligned} \quad (56)$$

The following parameters are defined to measure the intensity of the electromagnetic impacts

$$\lambda = \frac{e_{22}}{\kappa_{22}} \frac{D_0}{\sigma_0}; \quad \Lambda = \frac{h_{22}}{\gamma_{22}} \frac{B_0}{\sigma_0} \quad (57)$$

In standard implicit Newmark time integration, a sufficiently small time-step, e.g., $\Delta t = 1.05 \times 10^{-6}$ s, is chosen to ensure the accuracy of the results in the dynamics analysis. One must be noted that this time step has no effects on the stability of the implicit time integration scheme (Bui and Zhang, 2013; Bui and Zhang, 2012; Liu et al., 2013; Liu et al., 2014; Yu et al., 2015).

5.1. A central cracked MEE plate

To verify the accuracy of the developed XIGA, we consider a homogeneous, linear and rectangular multiphase MEE plate with a central crack of length $2a$ along x -axis as schematically depicted in Fig. 7. The geometric parameters of the MEE plate are $h = 20$ mm, $2w = h$, and $a = 2.4$ mm, where a represents a half-length of the crack.

For this example, we compare our cubic NURBS formulation (Degree 3 XIGA) to quadratic and bilinear NURBS approaches (Degrees 1 and 2 XIGA). Its purpose is to address the discretization effect with different orders of the NURBS basis functions. Fig. 8 shows a close-up of the distribution of enriched control points at the crack by different XIGA models using the degrees 1, 2 and 3 of the NURBS basis functions, respectively. It can be clearly observed from the figures that the enriched areas are different from each other. For a topological enrichment, "Degree

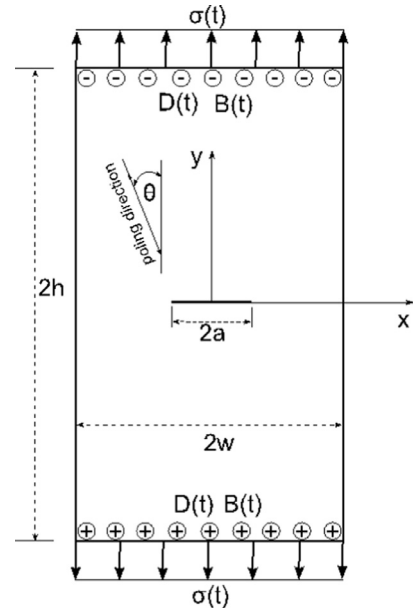


Fig. 7. Geometric notation of a rectangular MEE plate containing a central crack under coupled impact loading condition and arbitrary poling direction.

1 XIGA" has a smaller enrichment area compared to higher order XIGA formulations. It was shown by Dolbow (1999) in terms of XFEM that a topological enrichment leads to suboptimal convergence rates for this reason. A geometrical enrichment, that keeps the enriched domain constant during mesh refinement, can restore optimal convergence rates on cost of the conditioning of system stiffness matrix.

The higher models differentiate themselves and significantly reveal the advantages of the NURBS basis functions as the cracks are enriched by a larger area of enriched control points. It means that the enrichment domains change when varying the order of the NURBS (Bhardwaj et al., 2015). Since the Degree 3 XIGA with a large area of enriched domain is applied to solve all the numerical examples, we restrict our study by not considering the geometrical enrichment.

Although the geometrical enrichment can restore optimal convergence rates, enriching a fixed domain around the crack tip via the geometrical scheme however can give rise to several issues. As stated in Prange et al. (2012), because the enrichment functions are linearly constant inside the element for small elements away from the crack tip, a near linear dependence between the standard and enriched DOFs can thus be found. For refined meshes, the condition number of the coefficient matrix of the resulting algebraic equation system becomes large. Another difficulty may also be arisen when dealing with multiple cracks. In fact, it is not trivial to choose appropriate enrichment functions in case the crack fronts of multiple cracks come close (Prange et al., 2012).

In our dynamic study, the rectangular domain being examined is first discretized with several levels of physical meshes starting a coarse physical mesh, e.g., 17×47 elements, to the fine mesh, e.g., 77×137 elements. We have

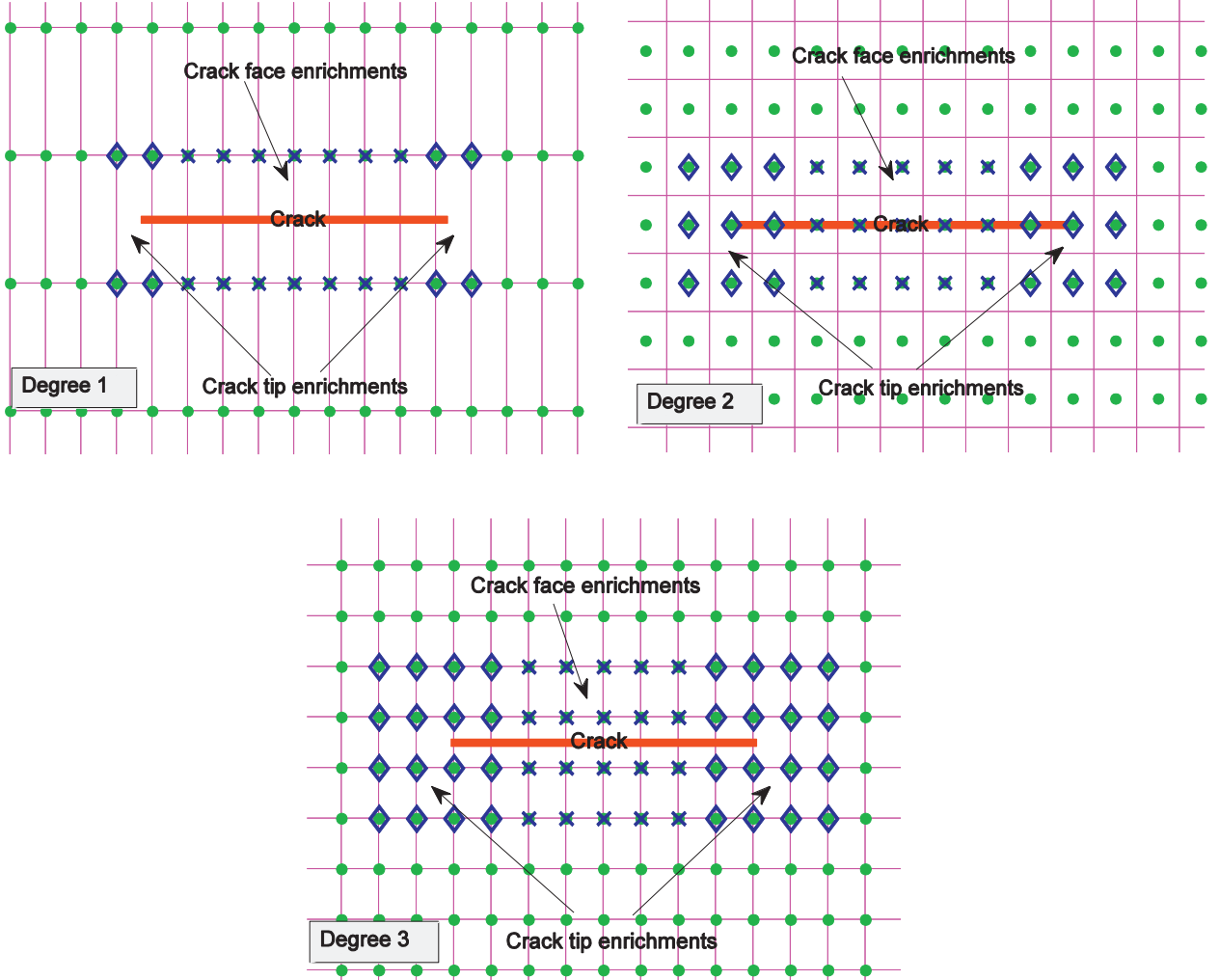


Fig. 8. Close-up of the distribution of enriched control points at the crack by different XIGA models using the degrees 1, 2 and 3 of the NURBS basis functions, respectively. Obviously the difference of the enriched areas among them is significant. While the degree 1 XIGA with uniform weights degenerating to the XFEM because of the unity degree of NURBS, the degrees 2 and 3 show the advantages of the higher-order degrees of the NURBS basis functions in terms of the enrichment XIGA.

found based on our own numerical experiments that at least a physical mesh of 40×80 elements is needed to attain acceptable result. The transient responses beyond this physical mesh density behave almost similar. For that reason we have used a fine physical mesh of 51×101 elements in this example to ensure the accuracy as well as to be computationally cost effective.

The normalized numerical results of different loading relations λ and Λ in Eq. (57) calculated by the proposed dynamic degree 3 XIGA using a fine physical mesh of 51×101 elements are shown in Fig. 9. The poling angle is set to be $\theta = 0^\circ$. Two cases of loading $\lambda = 0; \Lambda = 0$ and $\lambda = 1; \Lambda = 1$ are considered. The NDIFs K_I^* , K_{IV}^* and K_V^* show a very good agreement with the reference solutions obtained from the time domain boundary element method (TDBEM) (Wünsche et al., 2012) and the XFEM (Bui and Zhang, 2013). Note that the reference solution from the TDBEM (Wünsche et al., 2012) uses a uniform mesh with an element-length of 1.0 mm for the external boundary

and 12 elements for the crack face, while the XFEM (Bui and Zhang, 2013) solution uses a regular fine mesh of $70 \times 120 = 8400$ quadrilateral elements.

Under the applied loads as shown in Fig. 7, K_{II} vanishes since no shear stresses are induced. The analyses present very interesting results as they reveal a very different structure behavior between the pure mechanical load $\sigma_{22}(t) = \sigma_0 H(t)$ and a fully coupled magneto-electro-elastic impact load $\sigma_{22}(t) = \sigma_0 H(t)$, $D_2(t) = D_0 H(t)$, $B_2(t) = B_0 H(t)$. The transient responses induced by the coupled load $\lambda = 1; \Lambda = 1$ start from a non-zero value, indicating that the cracked MEE plate is immediately subjected to the magnetic and electric impacts and the crack hence opens at $t = 0$ (Wünsche et al., 2012; Bui and Zhang, 2013). The NDIFs under the pure mechanical load $\lambda = 0; \Lambda = 0$ however start from zero, and in this case the scattered elastic wave needs some time to reach and excite the crack. As explained in Wünsche et al. (2012) and Bui and Zhang (2013), this physical phe-

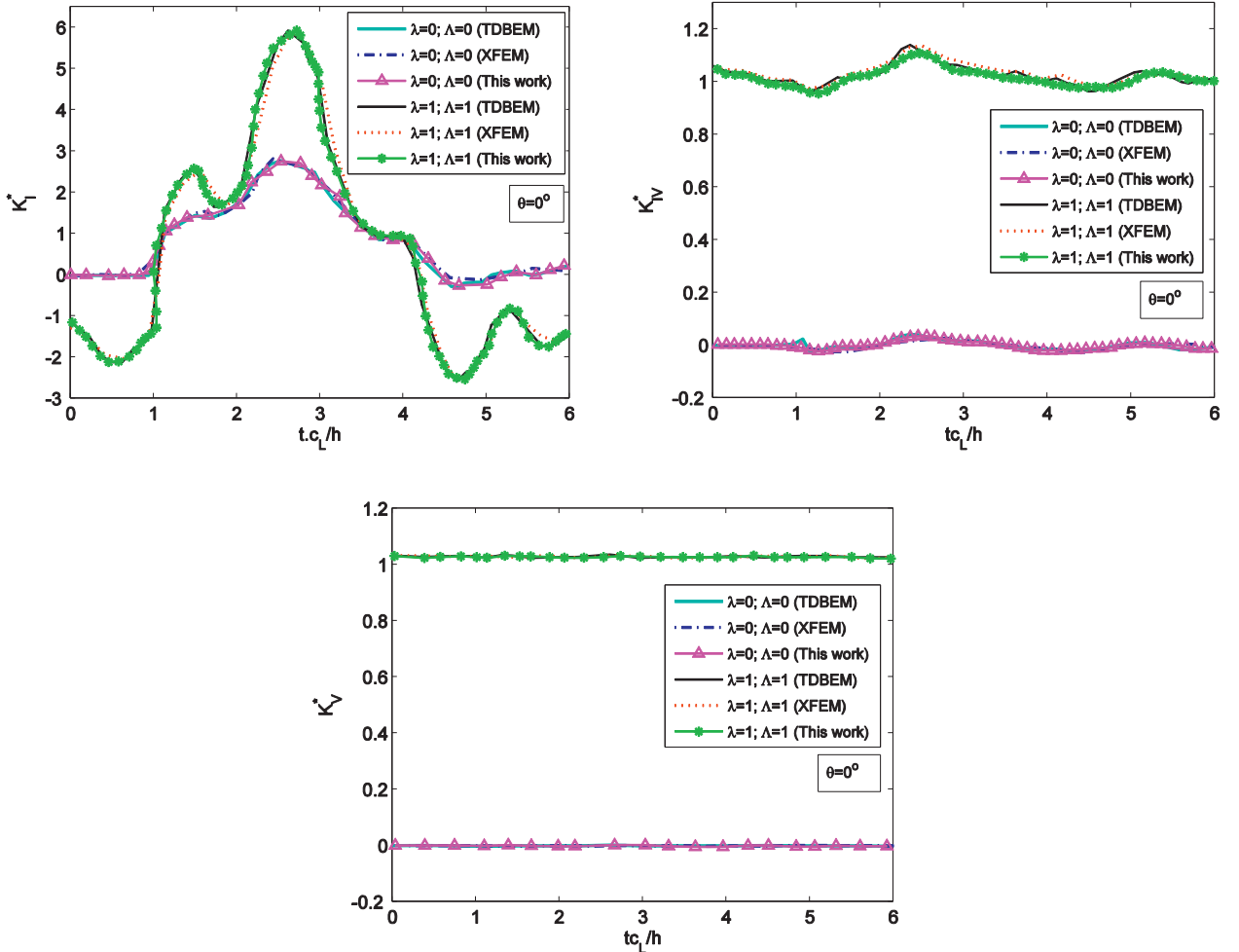


Fig. 9. Comparison of K_I^* , K_{IV}^* and K_V^* versus the normalized time for a central cracked MEE plate computed by the present XIGA, the TDBEM and the XFEM for different loading conditions.

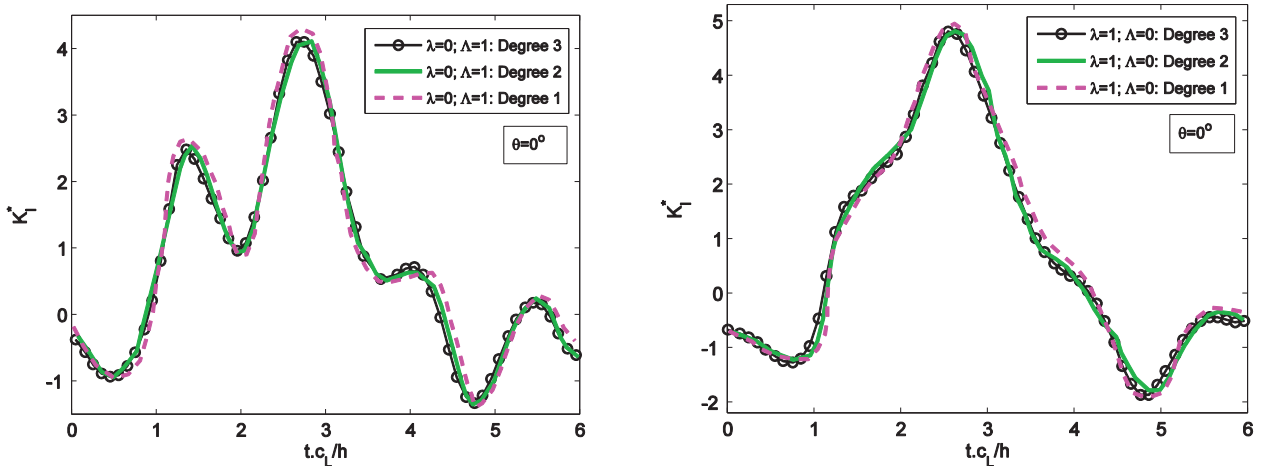


Fig. 10. Normalized extended dynamic stress intensity factors of a central crack versus normalized time under a pure electric loading ($D_2(t) = D_0H(t)$) and a pure magnetic loading ($B_2(t) = B_0H(t)$) for different orders of the NUBRS basis functions.

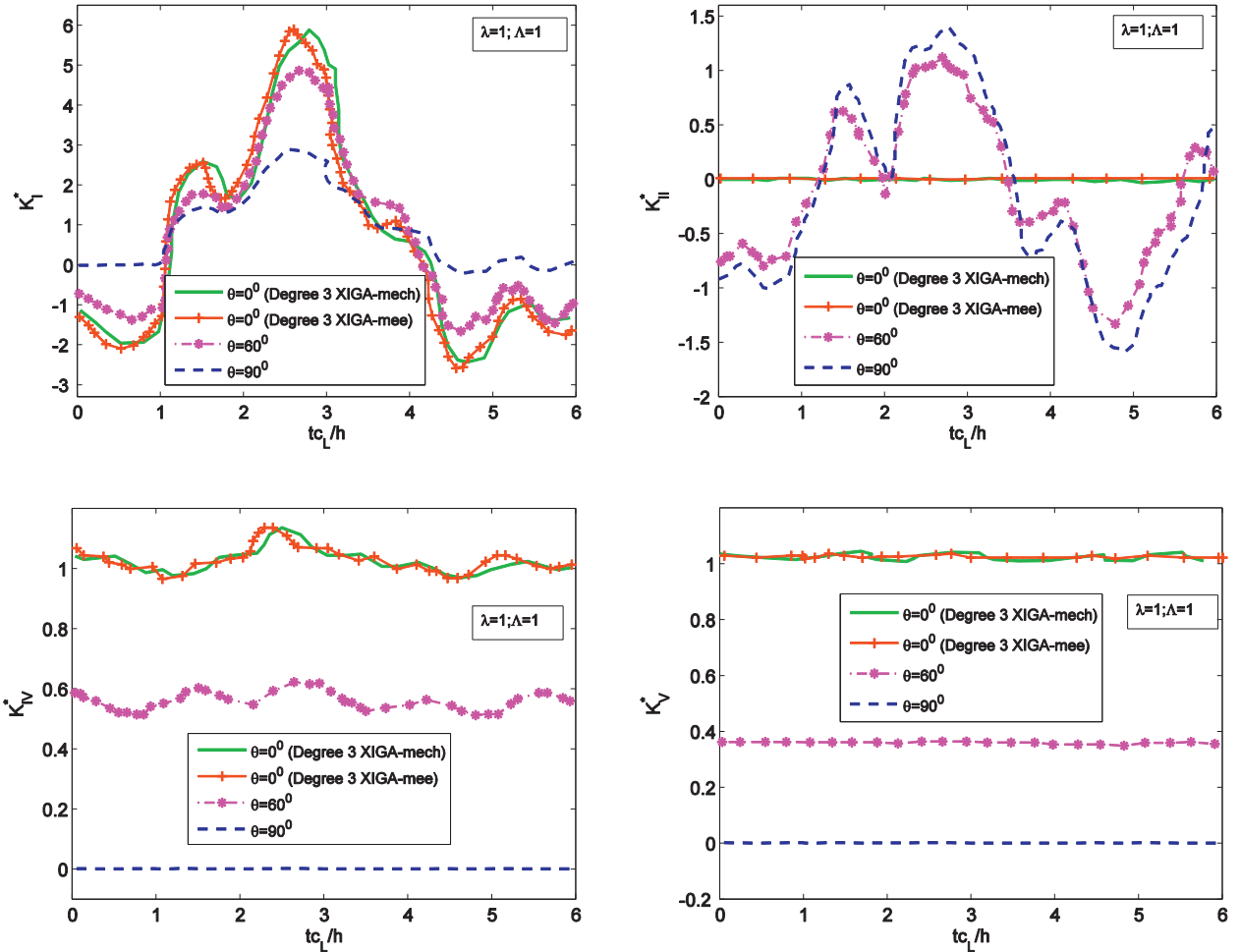


Fig. 11. Comparison of the transient responses of a central crack MEE plate obtained by the proposed XIGA for different rotation poling angles. Illustration of the effect of the enrichment functions on the normalized transient dynamic fracture parameters of a central crack MEE plate.

nomenon is due to the fact of the quasi-static assumption for the electrical and magnetic fields. Consequently those observed behaviors essentially reveal a strong effect of the electric and magnetic fields on the NDIFs in the cracked MEE materials.

The difference on the transient dynamic cracks caused by different loading conditions is a very important issue for the design and development of smart materials and structures. The maximum magnitude of the K_I^* , K_{II}^* and K_{III}^* responses caused by the coupled load $\lambda = 1; \Lambda = 1$ is larger than that by the mechanical load $\lambda = 0; \Lambda = 0$. The values of K_{II}^* and K_{III}^* gained by the pure mechanical load oscillate around zero, while that achieved by the coupled load oscillate around 1.0. As observed in the K_I^* response, it results in negative values within some small time intervals. The physically meaningless negative K_I^* may be caused by the non-contact assumption at the crack faces in the considered models, which may require an appropriate model and an advanced iterative solution procedure for simulating the crack-face contact problem.

For a poling direction of $\theta = 0^\circ$, Fig. 10 depicts the transient responses of the K_I^* versus the normalized time for different orders of the NURBS basis functions under a

pure electric impact load $\lambda = 1; \Lambda = 0$ and a pure magnetic load $\lambda = 0; \Lambda = 1$. The present results using a fine physical mesh of 51×101 elements show a good agreement among three models of degrees 1, 2 and 3 of the NURBS. The controllable accuracy of the responses altered by the orders of the basis functions is one of the major advantages of the proposed XIGA using NURBS, which substantially differs from the traditional methods like the XFEM. The behaviors of the responses under the applied loadings are very different between each other, but they all exhibit a non-zero value at $t = 0$, which is similar to the responses caused by the fully coupled load $\lambda = 1; \Lambda = 1$ as discussed above. From Figs. 9 and 10, it can easily be identified that the transient responses of the K_I^* increase with the electrical and magnetic loads.

It is important to stress out here that in general one can pick up the degree 2 for their analysis (note that the degree 1 is identical to the conventional FEM), which may have less DOFs than the degree 3. However, this is optimal and fully depends upon the analysts' experience. In this particular work, we decide to adopt the degree 3 for all the computations with the goal of achieving a fair accuracy of final numerical results.

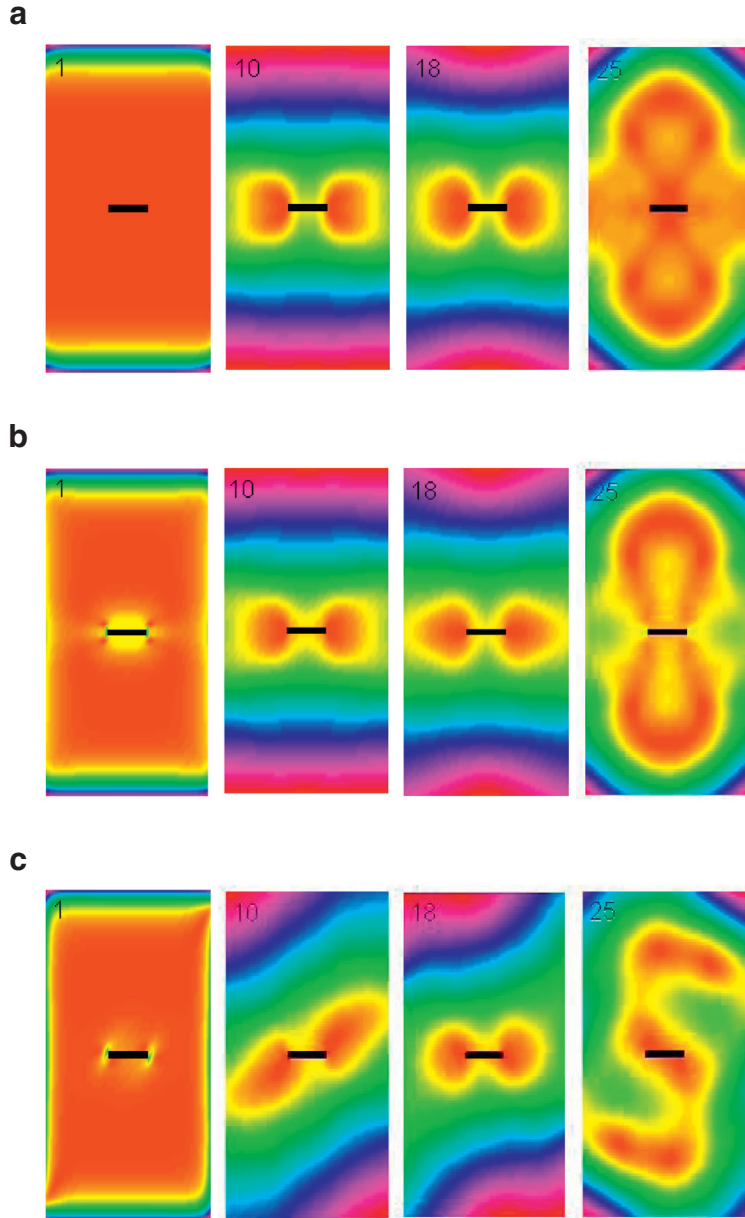


Fig. 12. Illustration of scattered elastic wave at different time steps obtained by the present degree 3 XIGA for a central crack MEE plate under different impact loading conditions: a pure mechanical load (a); a coupled electro-magneto-mechanical load (b) and (c); and different orientations of material poling direction: $\theta = 0^\circ$ (a), (b) and $\theta = 60^\circ$ (c).

In the following, the effects of the enrichment functions and the orientation of the material poling direction against y -axis and on the NDIFs are addressed. Generally the influence of the polarization on the dynamic responses of cracked MEE materials is significant as reported in Wünsche et al. (2012), Rojas-Díaz et al. (2011) and Bui and Zhang (2013). Basically the variation of the poling angle θ , as sketched in Fig. 7, can be adjusted to make the polarization in the materials differently at the crack faces. A comparison of the NDIFs for different poling angles, e.g., $\theta = 0^\circ$, 60° and 90° , under a fully coupled load

$\lambda = 1$; $\Lambda = 1$ is shown in Fig. 11. It is evident that the polarization direction greatly alters the transient responses. The behaviors under the poling effect are quite complicated. The increase of the poling angle leads to a decrease in the K_I^* , K_{IV}^* and K_V^* but increase in the K_{II}^* . In particular for the case of $\theta = 90^\circ$ the K_I^* is zero at the time $t = 0$ in which it needs some time to excite the crack, while the responses of K_{IV}^* and K_V^* are entirely zero because the piezoelectric/piezomagnetic effects vanish for a crack face tangential to the direction of polarization (Wünsche et al., 2012; Bui and Zhang, 2013).

To address the effect of the enrichment functions on the NDIFs, two different sets in Eqs. (28) and (33) termed as "Degree 3 XIGA-mee" and "Degree 3 XIGA-mech", respectively, are considered. The numerical results for $\theta = 0^\circ$ shown in Fig. 11 compare the dynamic responses between each other. Not surprisingly but interestingly the "Degree 3 XIGA-mech" can yield acceptable results as compared with the responses gained by the "Degree 3 XIGA-mee". Only a minor difference on the responses between two models is found. Although the "Degree 3 XIGA-mech" has been shown to be acceptable for use, the "Degree 3 XIGA-mee" is recommended in practice since it can fully capture all the characteristics of the singular fields at the crack tip and the polarization effects.

Fig. 12 further illustrates the insight into the behaviors of the transient responses by observing the propagation of the scattered elastic waves at different time steps. Here, two loading cases are considered. The pure mechanical load $\lambda = 1; \Lambda = 0$ is shown in Fig. 12a for a poling angle of $\theta = 0^\circ$, while the fully coupled load $\lambda = 1; \Lambda = 1$ is depicted in Fig. 12b and c for two polarization directions $\theta = 0^\circ$ and 60° , respectively. For the same poling angle of $\theta = 0^\circ$, the waves induced by different loads (see Fig. 12a and b) yield, in general, a similar behavior but in fact their intensities at the crack tip are different. More clearly, we can observe that the scattered waves propagating in the body at the time step 1 is very different between each other. The wave under $\lambda = 1; \Lambda = 0$ needs some time to reach and excite the crack whereas the wave under $\lambda = 1; \Lambda = 1$ immediately touches and opens the crack. When $\theta = 60^\circ$ is set and the same loading $\lambda = 1; \Lambda = 1$ is considered, the intensity and the behaviors of the scattered elastic waves are also very different from each other, see Fig. 12b and c. The applied loadings and polarization greatly alter the scattered elastic waves.

5.2. An inclined edge cracked MEE plate

In this example, we study a mixed-mode problem. A MEE plate with three edges supported and a slanted edge crack of length a at an angle $\alpha = 45^\circ$ aligned to the boundary is considered as depicted in Fig. 13. The geometrical parameters of plate are taken to be $w = 32$ mm, $h = 22$ mm, $c = 6$ mm and crack-length $a = 22.63$ mm. The plate is subjected to either a pure mechanical impact load ($\lambda = 0; \Lambda = 0$) or a fully coupled magneto-electro-elastic impact load ($\lambda = 1; \Lambda = 1$). The present transient results are compared to the reference solutions from XFEM, previously solved by the authors Bui and Zhang (2013).

Fig. 14 shows the comparison of transient responses of K_I^* , K_{II}^* , K_V^* and K_H^* calculated by the degree 3 XIGA and the existing XFEM solutions (Bui and Zhang, 2013). The degree 3 XIGA utilizes a fine physical mesh containing 61×101 elements, and the XFEM solutions (Bui and Zhang, 2013) are obtained utilizing a fine mesh with $70 \times 120 = 8400$ quadrilateral elements. The numerical results of the NDIFs are in good agreement. Under the prescribed loading and boundary conditions, the K_{II}^* can hence be developed. The impact loads greatly affecting the transient responses are again found. The NDIFs increase with the electric and magnetic loadings. Other similar phenomena as addressed in

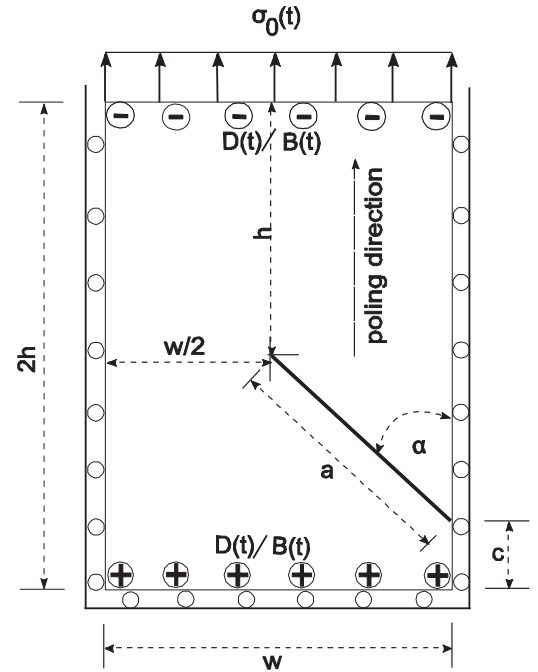


Fig. 13. Geometric notation of an inclined edge crack in a rectangular MEE plate under impact loading.

the previous example also can be observed in this example. For instance, the structure responses induced by the condition $\lambda = 1; \Lambda = 1$ start from a non-zero value in the beginning, which is in contrast to that induced by the condition $\lambda = 0; \Lambda = 0$. The behavior of transient responses can be observed more clearly in the scattered elastic waves at different time steps as visualized in Fig. 15. The produced elastic waves reveal a significant difference on the transient responses between the two distinct impact loads. The difference again can easily be distinguished at the first time step of the propagating waves. In contrast to the case of pure mechanical load where nothing happens to the crack in the beginning, the elastic wave under the coupled impact load immediately reaches and excited the crack.

5.3. Two equal parallel central cracks

The last numerical example considers a MEE plate with two equal parallel central cracks as shown in Fig. 16. The example demonstrates the applicability of the developed dynamic XIGA to model a cracked plate with complicated configuration. The crack interaction affecting the dynamic fracture parameters in multiphase MEE composites is also investigated. The geometrical parameters of the plate are $h = 16.0$ mm, $w = 20.0$ mm, and $a = 2.0$ mm. Each crack has a length of $2a$, and only two specific poling angles $\theta = 0^\circ$ and 45° as depicted in Fig. 16 are considered. Again, the pure mechanic load $\lambda = 0; \Lambda = 0$ and the fully combined impact load $\lambda = 1; \Lambda = 1$ are considered. We also introduce a parameter d as shown in Fig. 16 to indicate the distance between two cracks, and three values of $d = 3.0$, 6.0 and 10.0 mm are tested.

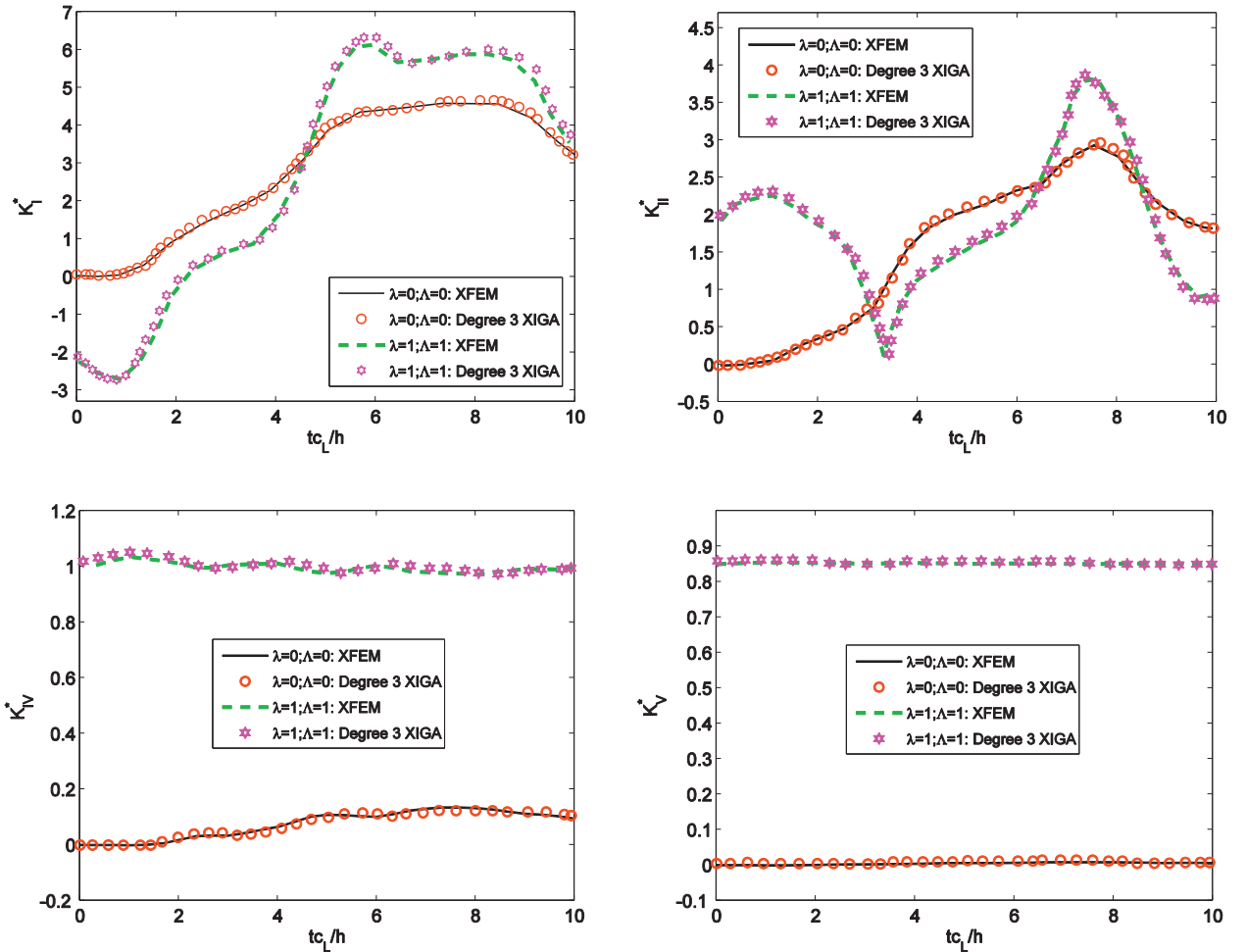


Fig. 14. Comparison of the normalized K_I^* , K_{IV}^* , K_V^* and K_{II}^* of a slanted edge crack for different impact loads between the proposed XIGA and the XFEM.

We first examine the effect of the polarization direction on the transient responses for different impact loads. We subsequently address the variation of the numerical results altered by the parameter d , and finally explore the finite size effect by considering different values of the crack-length-to-width ratio $a/w = 0.1, 0.25$ and 0.4 .

Because of the symmetry of the plate model including its boundary and loading conditions as well as two specified poling angles, we restrict our study by only measuring the numerical results for one crack tip. However, the transient responses at different crack tips may be different among each other if an arbitrary poling direction is considered. In this case, further investigations must be made.

Fig. 17 shows the polarization effect for two impact loads and two poling angles, i.e., $\theta = 0^\circ$ and 45° . A fine physical mesh consisting of 71×71 elements with $d = 6.0$ mm is used. We have observed consistent behaviors from the numerical results as discussed in the previous examples. As expected, the polarization and the impact loads greatly affect the transient dynamic responses. While the pure mechanical impact produces value which is approx-

imately zero in the beginning for the mode IV and mode V, the fully coupled impact load yields transient responses starting from a non-zero value.

As stated previously, we want to explore the effect of variation of the K_I^* , K_{IV}^* , K_V^* and K_{II}^* altering by d in this study. We select three different values of the distance $d = 3.0, 6.0$ and 10.0 mm for the analysis. The resulting numerical transient responses for different values of d are shown in Fig. 18 in which a poling angle of $\theta = 45^\circ$ and a fully coupled impact load $\lambda = 1 \Lambda = 1$ are taken. Overall, the parameter d has a large influence on the NDIFs. The larger the value of d is used the larger the amplitude of the NDIFs is obtained.

The above investigation has been done for a constant crack length of $a = 2.0$ mm. We now continue to conduct the study of finite size effect by considering different values of the aspect ratio a/w , and three typical values of the ratio given by $a/w = 0.1, 0.25$ and 0.5 . We also adopt $d = 6$ mm and $\theta = 45^\circ$ for this analysis. The results of different finite sizes are depicted in Fig. 19. As shown in Fig. 19, their transient responses are complicated and different. The results indicate that the finite size plays a

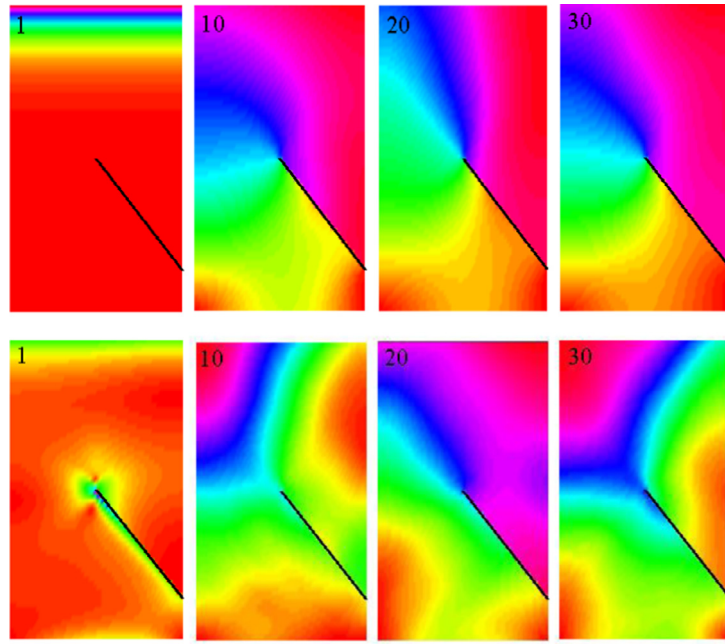


Fig. 15. Illustration of scattered elastic wave at different time steps obtained by the present degree 3 XIGA for a slanted edge crack under a pure mechanical load $\lambda = 0 \Lambda = 0$ and a coupled load $\lambda = 1 \Lambda = 1$.

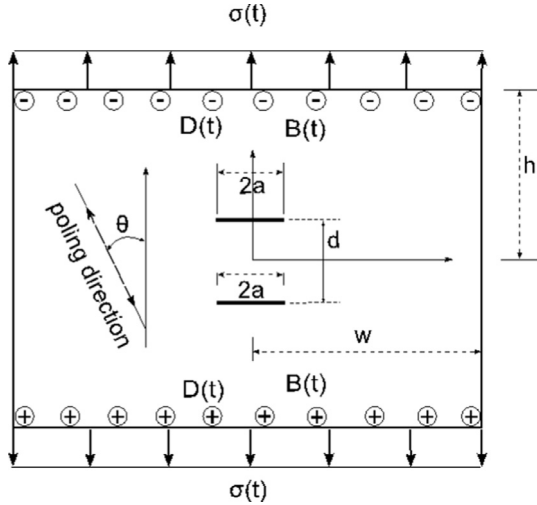


Fig. 16. Geometric notation of a rectangular MEE plate containing two equal parallel cracks under impact load.

role in the dynamic fracture analysis of MEE plate and its effect is obvious.

The scattered elastic waves propagating in the plate are visualized in Fig. 20. More precisely, Fig. 20 shows a comparison of the scattered elastic wave at different time steps obtained by the cubic XIGA formulation for $d=6\text{ mm}$. A total of five cases are shown in Fig. 20. They are (a) $\lambda = 0 \Lambda = 0, \theta = 0^\circ; a/w = 0.1$; (b) $\lambda = 1 \Lambda = 1, \theta = 0^\circ, a/w = 0.1$; (c) $\lambda = 1 \Lambda = 1, \theta = 45^\circ, a/w = 0.1$; (d) $\lambda = 1 \Lambda = 1, \theta = 45^\circ, a/w = 0.25$; and (e) $\lambda = 1 \Lambda = 1, \theta = 45^\circ$,

$a/w = 0.5$. It is interesting to observe as the crack length increases the peak on the response of K_i^* disappears.

All the numerical results investigated above have been made employing a volume fraction $v_f = 0.5$ of BaTiO₃-CoFe₂O₄. The volume fraction of the MEE materials however may vary the transient response of NDIFs, and this effect is thus explored here. To this end, a MEE plate with two equal parallel cracks ($a = 2.0\text{ mm}$ and $d = 6.0\text{ mm}$) is again considered. We assume that the MEE plate under consideration is subjected to a fully coupled impact load $\lambda = 1 \Lambda = 1$, suffering a poling angle of $\theta = 0^\circ$. The MEE plate being studied is made of BaTiO₃-CoFe₂O₄ in which BaTiO₃ stands for the inclusion and CoFe₂O₄ as the matrix. The volume fraction of the inclusions is denoted by v_f . The material constants of the piezomagnetic (CoFe₂O₄) matrix and piezoelectric inclusion BaTiO₃ are listed in Table 2 (Song and Sih, 2003). To estimate the volume fractions in the MEE composites, the rule-of-mixture given by $\hbar_{ij}^c = \hbar_{ij}^i v_f + \hbar_{ij}^m (1 - v_f)$ is taken, where the superscripts c, i and m represent as the composite, inclusion and matrix, respectively. The term \hbar_{ij} can stand for $C_{ij}, e_{ij}, \kappa_{ij}, h_{ij}$ and γ_{ij} . Large volume fraction implies that the characteristic of the plate suffers more and more piezoelectric effect, and whereas small means more piezomagnetic effect.

Fig. 21 finally shows the computed transient results of the NDIFs accounted for different volume fractions, e.g., $v_f = 0.2, 0.4, 0.6$, and 0.8 . In the analysis, the mass densities corresponding to each volume fraction are respectively taken as $\rho(\text{kg/m}^3) = 5400; 5500; 5600$ and 5700 . To obtain concrete results, all the computations are performed using the degree 3 XIGA with a fine physical mesh

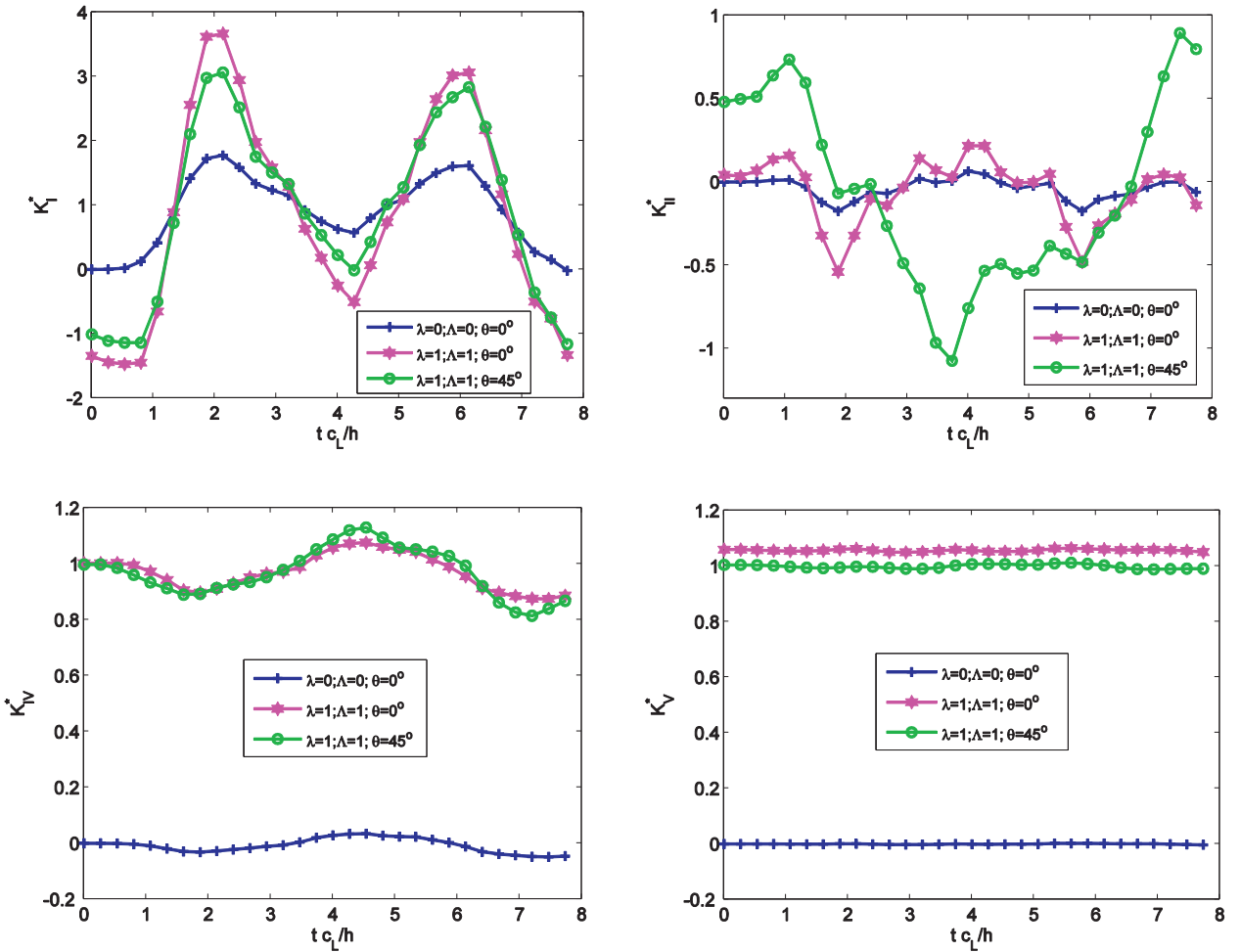


Fig. 17. The effect of polarization on the NDIFs of a MEE plate with two equal parallel cracks for different impact loads.

of 71×71 elements. The gained numerical transients of the NDIFs are very interesting. It is apparently that altering the volume fraction leads to a significant variation of the transient responses of NDIFs, and that situation can be observed clearer beyond the normalized time of 2. The effect occurred after that period (i.e., 2) is insignificant. By increasing the volume fraction the amplitudes of the responses increase in some ranges and decrease in some other ranges, e.g., see mode I. Due to the coupled loading effect, the mode II behaviors greatly oscillate around zero, but the values of mode II are non-zero. Also, the curves of mode I start from non-zero, which is induced by the coupled load as well, and this issue has already been stated out in the previous examples. A great variation of the mode IV and mode V by altering the volume fraction can also be seen clearly in the figures. Overall the transient responses of the NDIFs behave almost similar for different volume fractions. Once $\nu_f = 0.2$ is taken, for which a large oscillation and different behavior compared to other cases is found. Loosely speaking, the oscillation induced by $\nu_f = 0.2$ may be due to the fact that high volume frac-

tion of MEE material leads to material constants equivalent to piezoelectric ceramic, and the electric-mechanical coupling may have more diverse effect on the NDIFs than the magneto-electro-mechanical one.

The transient responses of NDIFs for different multiphase compositions of piezoelectric/piezomagnetic obtained the developed XIGA are analyzed. Except materials, other information regarding the plate such as the geometry, poling angle $\theta = 0^\circ$, two equal parallel cracks with $a = 2.0\text{mm}$ and $d = 6.0\text{ mm}$, is taken. To this end, the following inclusions materials of piezoelectric phase such as PECP (PZT-epoxy mixed component) (Liu et al., 2003), PZT-4 (Rajapakse, 1997), and PZT-6B (Rajapakse, 1997) with the same matrix piezomagnetic phase of CoFe_2O_4 are considered. Their detailed material parameters are listed in Table 2. A volume fraction of $\nu_f = 0.5$ is considered, where all material constants of the three considered MEE material plates are determined through the aid of the rule-of-mixture addressed above. Also, a mass density of $\rho = 5500\text{ kg/m}^3$ is applied to all specified MEE materials. Fig. 22 depicts the computed numerical transient responses of

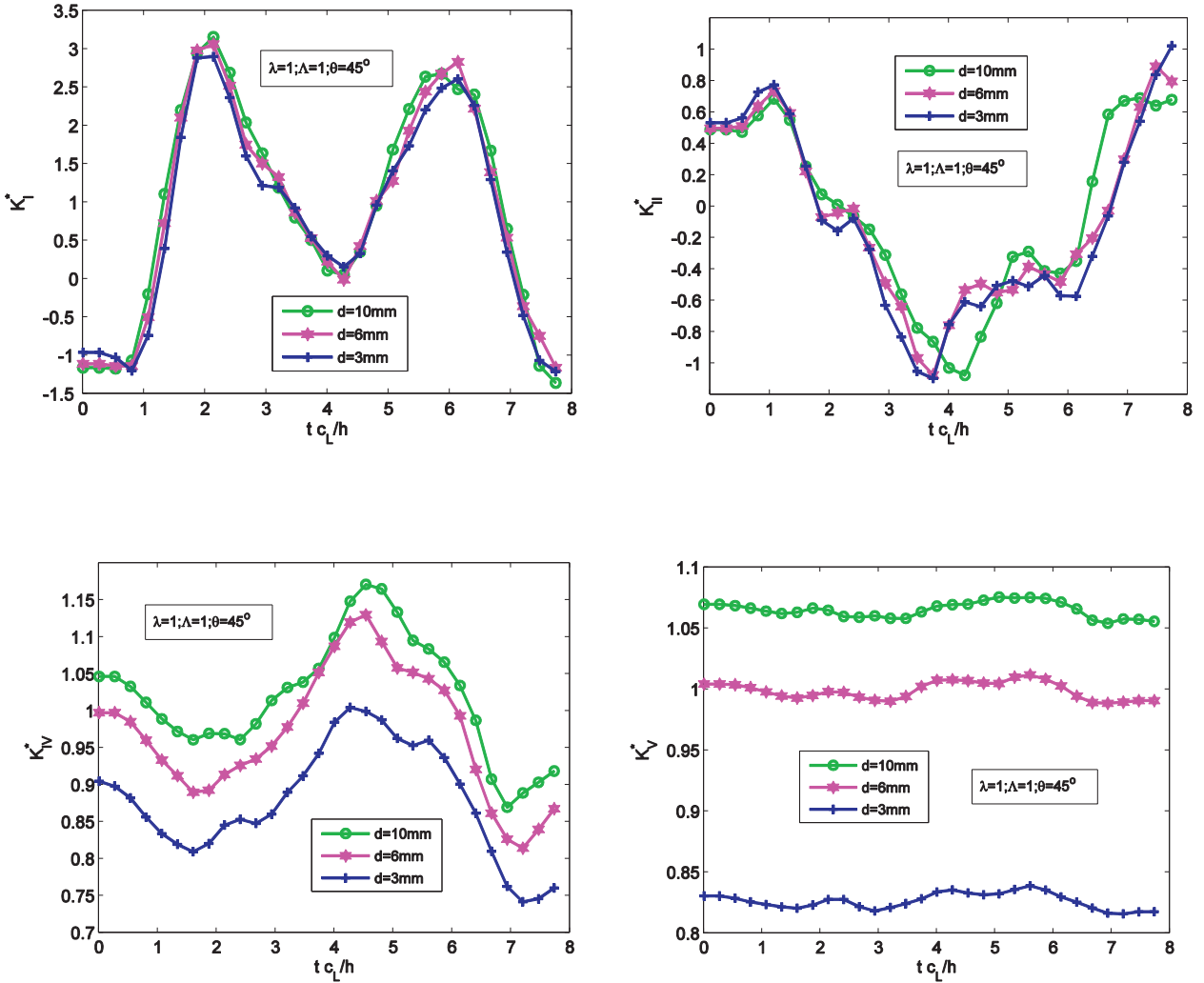


Fig. 18. Variation of the NDIFs of a MEE plate with two equal parallel cracks under a fully coupled impact load $\lambda = 1$, $\Lambda = 1$, and $\theta = 45^\circ$ for different values of the distance d .

such three MEE materials for the fully coupled load ($\lambda = 1$; $\Lambda = 1$) and the pure mechanical one ($\lambda = 0$; $\Lambda = 0$) using the degree 3 XIGA with a fine mesh of 71×71 elements. As expected, reasonable numerical results under the mechanical load can be observed as their calculated curves start from zero, whereas it is found differently from those induced by the coupled load. More interestingly, the amplitudes of NDIFs of MEE plates produced under the coupled load are larger than those under the mechanical one.

6. Conclusions and outlook

An accurate extended isogeometric analysis has been developed for the dynamic fracture modeling of electrically and magnetically impermeable cracks in multiphase MEE composite materials. We have used the NURBS basis functions, which are simultaneously used for the geometrical description and the approximation of the unknown field

variables. To handle the singularity at the crack tip, the asymptotic crack tip enrichment functions for MEE materials are taken, while the Heaviside function is employed to describe the discontinuity at the crack faces. The present method in which the entire crack to be modeled independent of the finite element mesh is found to be accurate and effective, showing one of the desirable characteristics of the XIGA in simulating cracks, as a result of locally enriched isogeometric approximation by enrichment functions and high-order continuity of the NURBS basis functions. The dynamic extended fracture parameters of cracked MEE solids are measured through the interaction integral considering the inertial effect. Some major conclusions drawn from our numerical investigation can be summarized as follows:

- The high accuracy of the transient dynamic cracks obtained by the proposed XIGA has been illustrated and demonstrated in the numerical results through three

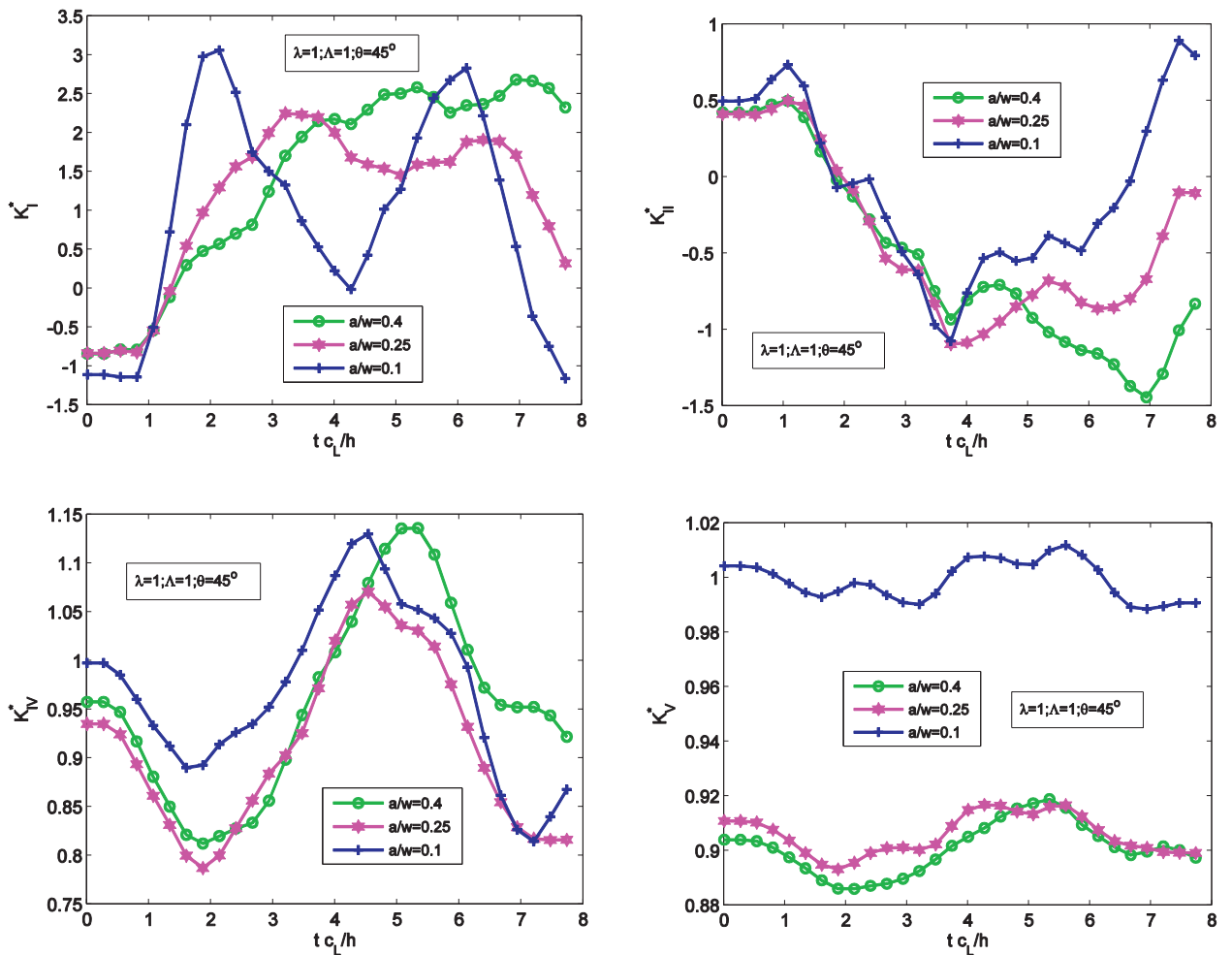


Fig. 19. Finite size effect on the NDIFs of a MEE plate with two equal parallel cracks under a fully coupled impact load $\lambda = 1$, $\Delta = 1$ and $\theta = 45^\circ$.

examples including single and mixed-mode fractures. It is found that the influences of the polarization, finite size and the loading conditions on the transient responses are significant to the solution.

- Different orders of the NURBS basis functions, up to 3 for instance, have been examined and a good agreement among models of the degree 1, 2 and 3 is found. The use of higher-order NURBS basis functions is a major advantage in the present formulation as the accuracy of the transient dynamic cracks can be controlled and improved.
- In multiple two-parallel cracks, the finite size effect reveals clearly and distinctly in the computed dynamic responses, while the distance parameter between the two cracks is found to be greatly altering the dynamic fracture behaviors.
- Significant variations of the transient responses of the NDIFs by altering volume fraction of MEE materials are found.
- The transient responses of NDIFs accounting for different multiphase compositions of piezoelec-

tric/piezomagnetic are investigated and reasonable results are obtained.

- It is observed in our own numerical study that the dynamic crack behaviors in multiphase MEE materials are much more complicated than those of constitute materials, and the result of this work may be helpful in the design and development of smart materials in engineering applications.

Although the main advantage of the enrichment method is its ability in simulating the crack growth without the need for re-meshing, this work however is our first attempt to the development of an accurate dynamic XIGA using the NURBS basis functions for transient responses modeling of stationary cracks in MEE solids subjected to coupled impact loading. Other problems like dynamic crack propagation or interface cracks (Lei et al., 2015; Lei et al., 2015) in MEE or graded MEE materials would be possible and should be addressed in the future.

Another interesting approach replacing the NURBS basis functions by T-spline basis functions (Ghorashi et al., 2015),

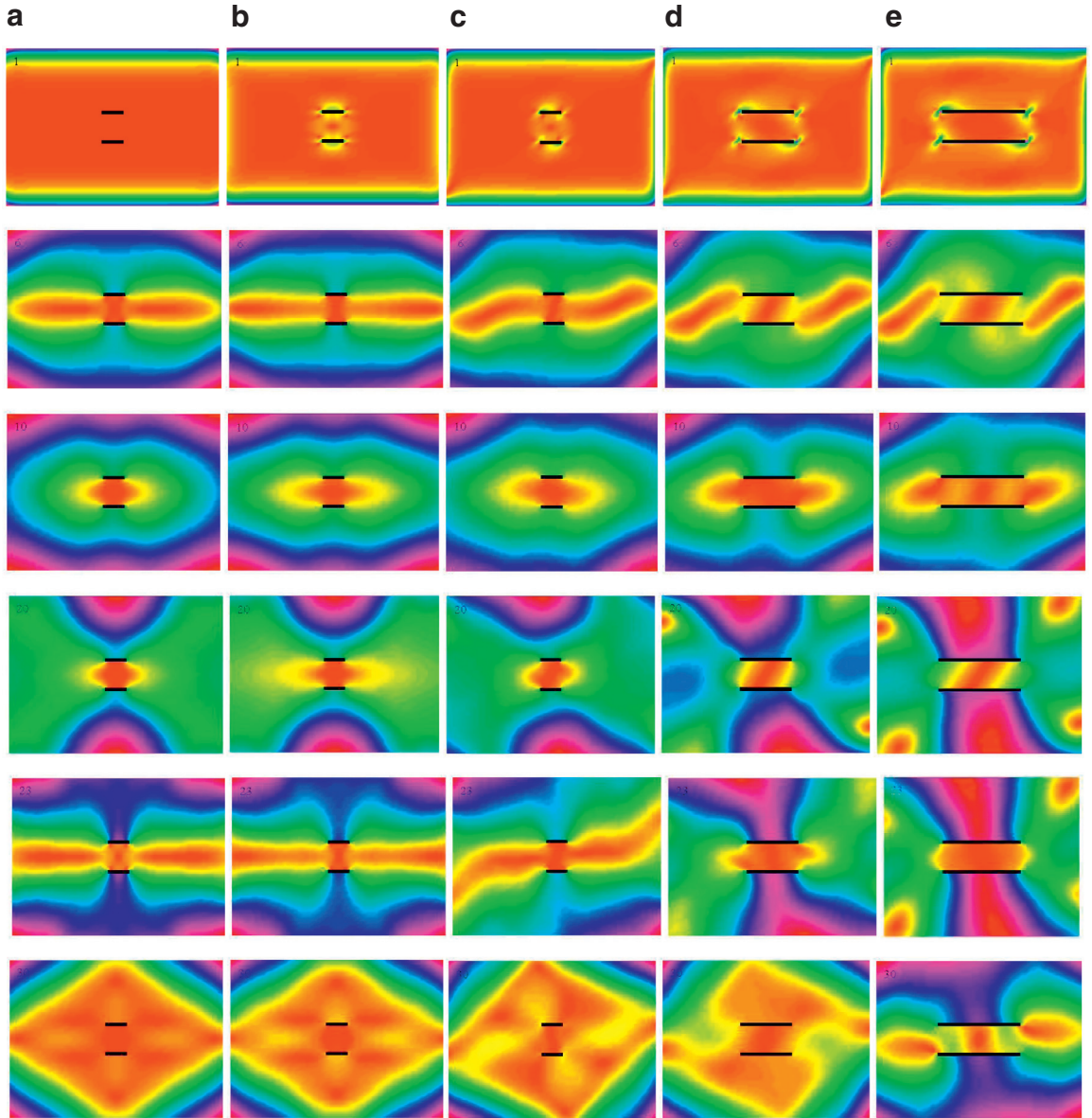


Fig. 20. Illustration of scattered elastic wave at different time steps obtained by the present degree 3 XIGA for a MEE plate with two equal parallel cracks with $d = 6$ mm: (a) $\lambda = 0$, $\Delta = 0$, $\theta = 0^\circ$, $a/w = 0.1$; (b) $\lambda = 1$, $\Delta = 1$, $\theta = 0^\circ$, $a/w = 0.1$; (c) $\lambda = 1$, $\Delta = 1$, $\theta = 45^\circ$, $a/w = 0.1$; (d) $\lambda = 1$, $\Delta = 1$, $\theta = 45^\circ$, $a/w = 0.25$; and (e) $\lambda = 1$, $\Delta = 1$, $\theta = 45^\circ$, $a/w = 0.5$.

which are highly suitable for refinements by means of the IGA, would be potential in fracture modeling of smart materials and structures as well.

Since our main objective is to deal with the straight cracks, the modeling of curved crack problems is not considered in the present MEE work. Therefore, further developments for curved cracks in MEE materials and structures are necessary.

Also in future works, the ill-conditioned system of equations must be taken into account when dealing with the evolution of crack on a fixed physical mesh where the crack may place very close to the element edges. The

ill-conditioned problem may also give rise to once handling a fixed enriched area, i.e., geometrical enrichment. To circumvent this ill-conditioned circumstance, a special technique is required, for instance, the pre-conditioners (Bechet et al., 2005; Strouboulis et al., 2000) or gathering method to decrease the number of unknowns and the condition number in fracture problems (Laborde et al., 2005), or a special algorithm of solving the system of linear equations (Riley, 1955), and so on.

The non-linear electric and magnetic crack-face boundary conditions as well as the contact at the crack-faces should be taken into account in our further developments.

Table 2

Material constants for BaTiO₃ and CoFe₂O₄ (Song and Sih, 2003); PECP (Liu et al., 2003); PZT-4 and PZT-6B (Rajapakse, 1997).

Matrix Properties	CoFe ₂ O ₄	Inclusions			
		BaTiO ₃	PECP	PZT-4	PZT-6B
C_{11} (GPa)	286	166	79.7	139	168
C_{12} (GPa)	170	78	35.8	77.8	60
C_{22} (GPa)	269.5	162	66.8	115	163
C_{66} (GPa)	45.3	43	17.2	25.6	27.1
e_{21} (C/m ²)	0	11.6	10.5	-5.2	-0.9
e_{22} (C/m ²)	0	-4.4	15.2	15.1	7.1
e_{16} (C/m ²)	0	18.6	-5.9	12.7	4.6
$\kappa_{11} (\times 10^{-10} \text{C}^2/\text{Nm}^2)$	0.08	11.2	15.92	6.46	3.6
$\kappa_{22} (\times 10^{-10} \text{C}^2/\text{Nm}^2)$	0.093	12.6	15.92	5.62	3.4
h_{21} (N/Am)	550	0	0	0	0
h_{22} (N/Am)	580.3	0	0	0	0
h_{16} (N/Am)	699.7	0	0	0	0
$\gamma_{11} (\times 10^{-6} \text{Ns}^2/\text{C}^2)$	-590	5	0	0	0
$\gamma_{22} (\times 10^{-6} \text{Ns}^2/\text{C}^2)$	157	10	0	0	0

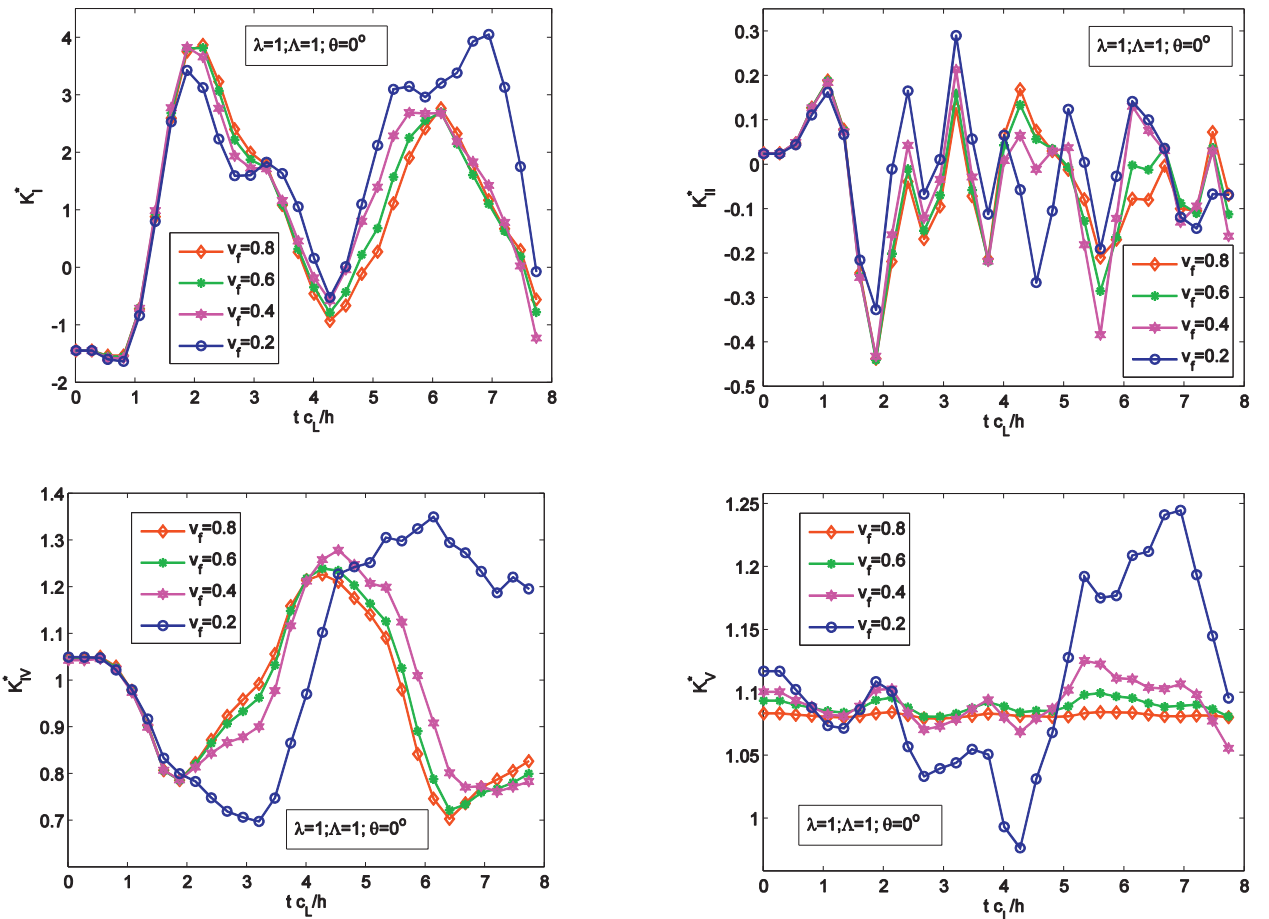


Fig. 21. Variation of the NDIFs of MEE plates with two equal parallel cracks ($a = 2.0$ mm and $d = 6.0$ mm) under a fully coupled impact load $\lambda = 1\Lambda = 1$, and $\theta = 0^\circ$ for different volume fractions.

Detection of flaws (e.g., single or multiple cracks and voids) in MEE materials in the context of inverse problems by combination of the proposed XIGA and multilevel coordinate search (MCS), see Nanthakumar et al. (2013) and

Nanthakumar et al. (2014) for piezoelectric materials with XFEM, would be potential. In this direction, the capability of representing complex geometries of the NURBS would be of great advantages.

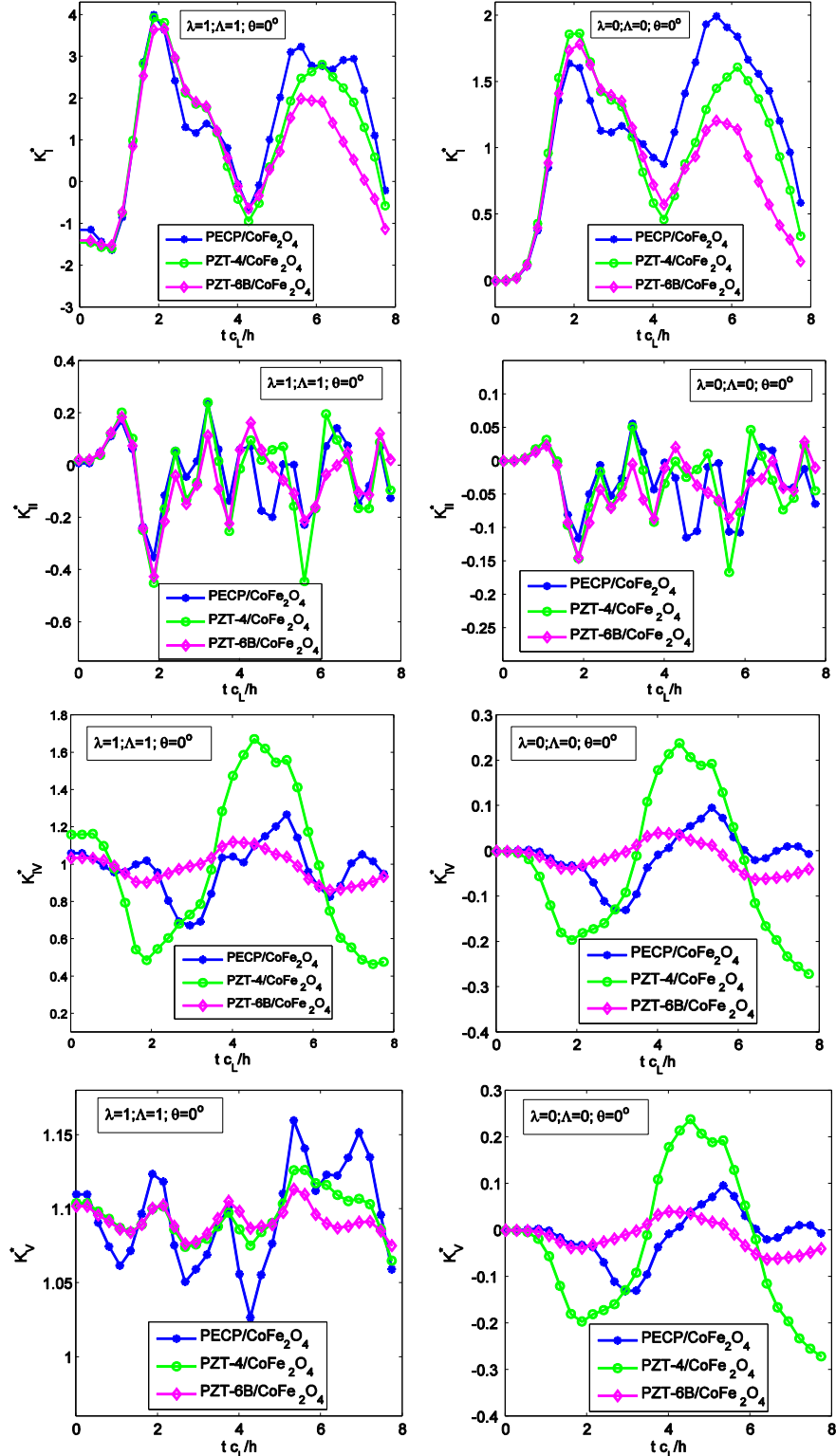


Fig. 22. Variation of NDIFs of three different MEE plates (PECP/CoFe₂O₄; PZT-4/CoFe₂O₄; PZT-6B/CoFe₂O₄) under fully coupled ($\lambda = 1 \Lambda = 1$) and pure mechanical ($\lambda = 0; \Lambda = 0$) loads.

Acknowledgments

The financial supports of the Grant-in-Aid for Scientific Research (No. 26-04055) – Japan Society for the Promotion of Sciences (JSPS, ID No. P14055), the German Research Foundation (DFG, Project-No. ZH 15/14-1), and the National Natural Science Foundation of China under Grant No. 11472021, are gratefully acknowledged. The authors would like to thank all anonymous reviewers for their insightful comments that help improve the manuscript.

Appendix A

The components of the stiffness matrices

$$\begin{aligned} \mathbf{K}_{mm}^{uu} &= \int_{\Omega^{[e]}} (\mathbf{B}_I^u)^T \mathbf{C} \mathbf{B}_J^u d\Omega; \\ \mathbf{K}_{mm}^{u\alpha} &= \mathbf{K}_{mm}^{\alpha u} = \int_{\Omega^{[e]}} (\mathbf{B}_I^u)^T \mathbf{C} \mathbf{B}_J^\alpha d\Omega; \\ \mathbf{K}_{mm}^{u\beta} &= \mathbf{K}_{mm}^{\beta u} = \int_{\Omega^{[e]}} (\mathbf{B}_I^u)^T \mathbf{C} \mathbf{B}_J^\beta d\Omega; \\ \mathbf{K}_{mm}^{\alpha\alpha} &= \int_{\Omega^{[e]}} (\mathbf{B}_I^\alpha)^T \mathbf{C} \mathbf{B}_J^\alpha d\Omega; \\ \mathbf{K}_{mm}^{\alpha\beta} &= \mathbf{K}_{mm}^{\beta\alpha} = \int_{\Omega^{[e]}} (\mathbf{B}_I^\alpha)^T \mathbf{C} \mathbf{B}_J^\beta d\Omega; \\ \mathbf{K}_{mm}^{\beta\beta} &= \int_{\Omega^{[e]}} (\mathbf{B}_I^\beta)^T \mathbf{C} \mathbf{B}_J^\beta d\Omega \end{aligned} \quad (A.1)$$

$$\begin{aligned} \mathbf{K}_{me}^{uu} &= \int_{\Omega^{[e]}} (\mathbf{B}_I^u)^T \mathbf{e} \mathbf{B}_J^u d\Omega; \\ \mathbf{K}_{me}^{u\alpha} &= \mathbf{K}_{me}^{\alpha u} = \int_{\Omega^{[e]}} (\mathbf{B}_I^u)^T \mathbf{e} \mathbf{B}_J^\alpha d\Omega; \\ \mathbf{K}_{me}^{u\beta} &= \mathbf{K}_{me}^{\beta u} = \int_{\Omega^{[e]}} (\mathbf{B}_I^u)^T \mathbf{e} \mathbf{B}_J^\beta d\Omega; \\ \mathbf{K}_{me}^{\alpha\alpha} &= \int_{\Omega^{[e]}} (\mathbf{B}_I^\alpha)^T \mathbf{e} \mathbf{B}_J^\alpha d\Omega; \\ \mathbf{K}_{me}^{\alpha\beta} &= \mathbf{K}_{me}^{\beta\alpha} = \int_{\Omega^{[e]}} (\mathbf{B}_I^\alpha)^T \mathbf{e} \mathbf{B}_J^\beta d\Omega; \\ \mathbf{K}_{me}^{\beta\beta} &= \int_{\Omega^{[e]}} (\mathbf{B}_I^\beta)^T \mathbf{e} \mathbf{B}_J^\beta d\Omega \end{aligned} \quad (A.2)$$

$$\begin{aligned} \mathbf{K}_{em}^{uu} &= \mathbf{K}_{me}^{uu}; \quad \mathbf{K}_{em}^{u\alpha} = \mathbf{K}_{em}^{\alpha u} = \mathbf{K}_{me}^{u\alpha} = \mathbf{K}_{me}^{\alpha u}; \\ \mathbf{K}_{em}^{u\beta} &= \mathbf{K}_{em}^{\beta u} = \mathbf{K}_{em}^{u\beta} = \mathbf{K}_{me}^{\beta u}; \quad \mathbf{K}_{em}^{\alpha\alpha} = \mathbf{K}_{me}^{\alpha\alpha}; \\ \mathbf{K}_{em}^{\alpha\beta} &= \mathbf{K}_{em}^{\beta\alpha} = \mathbf{K}_{me}^{\alpha\beta} = \mathbf{K}_{me}^{\beta\alpha}; \quad \mathbf{K}_{em}^{\beta\beta} = \mathbf{K}_{me}^{\beta\beta} \end{aligned} \quad (A.3)$$

$$\begin{aligned} \mathbf{K}_{m\bar{m}}^{uu} &= \int_{\Omega^{[e]}} (\mathbf{B}_I^u)^T \mathbf{h} \mathbf{B}_J^u d\Omega; \\ \mathbf{K}_{m\bar{m}}^{u\alpha} &= \mathbf{K}_{m\bar{m}}^{\alpha u} = \int_{\Omega^{[e]}} (\mathbf{B}_I^u)^T \mathbf{h} \mathbf{B}_J^\alpha d\Omega; \\ \mathbf{K}_{m\bar{m}}^{u\beta} &= \mathbf{K}_{m\bar{m}}^{\beta u} = \int_{\Omega^{[e]}} (\mathbf{B}_I^u)^T \mathbf{h} \mathbf{B}_J^\beta d\Omega; \\ \mathbf{K}_{m\bar{m}}^{\alpha\alpha} &= \int_{\Omega^{[e]}} (\mathbf{B}_I^\alpha)^T \mathbf{h} \mathbf{B}_J^\alpha d\Omega; \\ \mathbf{K}_{m\bar{m}}^{\alpha\beta} &= \mathbf{K}_{m\bar{m}}^{\beta\alpha} = \int_{\Omega^{[e]}} (\mathbf{B}_I^\alpha)^T \mathbf{h} \mathbf{B}_J^\beta d\Omega; \\ \mathbf{K}_{m\bar{m}}^{\beta\beta} &= \int_{\Omega^{[e]}} (\mathbf{B}_I^\beta)^T \mathbf{h} \mathbf{B}_J^\beta d\Omega \end{aligned} \quad (A.4)$$

$$\mathbf{K}_{\bar{m}\bar{m}}^{uu} = \mathbf{K}_{m\bar{m}}^{uu}; \quad \mathbf{K}_{\bar{m}\bar{m}}^{u\alpha} = \mathbf{K}_{\bar{m}\bar{m}}^{\alpha u} = \mathbf{K}_{m\bar{m}}^{u\alpha} = \mathbf{K}_{m\bar{m}}^{\alpha u};$$

$$\begin{aligned} \mathbf{K}_{\bar{m}\bar{m}}^{u\beta} &= \mathbf{K}_{\bar{m}\bar{m}}^{\beta u} = \mathbf{K}_{\bar{m}\bar{m}}^{\beta\alpha} = \mathbf{K}_{m\bar{m}}^{\beta\alpha}; \quad \mathbf{K}_{\bar{m}\bar{m}}^{\alpha\alpha} = \mathbf{K}_{m\bar{m}}^{\alpha\alpha}; \\ \mathbf{K}_{\bar{m}\bar{m}}^{\alpha\beta} &= \mathbf{K}_{\bar{m}\bar{m}}^{\beta\alpha} = \mathbf{K}_{m\bar{m}}^{\alpha\beta} = \mathbf{K}_{m\bar{m}}^{\beta\alpha}; \quad \mathbf{K}_{\bar{m}\bar{m}}^{\beta\beta} = \mathbf{K}_{m\bar{m}}^{\beta\beta} \end{aligned} \quad (A.5)$$

$$\begin{aligned} \mathbf{K}_{ee}^{uu} &= \int_{\Omega^{[e]}} (\mathbf{B}_I^u)^T \kappa \mathbf{B}_J^u d\Omega; \\ \mathbf{K}_{ee}^{u\alpha} &= \mathbf{K}_{ee}^{\alpha u} = \int_{\Omega^{[e]}} (\mathbf{B}_I^u)^T \kappa \mathbf{B}_J^\alpha d\Omega; \\ \mathbf{K}_{ee}^{u\beta} &= \mathbf{K}_{ee}^{\beta u} = \int_{\Omega^{[e]}} (\mathbf{B}_I^u)^T \kappa \mathbf{B}_J^\beta d\Omega; \\ \mathbf{K}_{ee}^{\alpha\alpha} &= \int_{\Omega^{[e]}} (\mathbf{B}_I^\alpha)^T \kappa \mathbf{B}_J^\alpha d\Omega; \\ \mathbf{K}_{ee}^{\alpha\beta} &= \mathbf{K}_{ee}^{\beta\alpha} = \int_{\Omega^{[e]}} (\mathbf{B}_I^\alpha)^T \kappa \mathbf{B}_J^\beta d\Omega; \\ \mathbf{K}_{ee}^{\beta\beta} &= \int_{\Omega^{[e]}} (\mathbf{B}_I^\beta)^T \kappa \mathbf{B}_J^\beta d\Omega \end{aligned} \quad (A.6)$$

$$\begin{aligned} \mathbf{K}_{em}^{uu} &= \int_{\Omega^{[e]}} (\mathbf{B}_I^u)^T \beta \mathbf{B}_J^u d\Omega; \\ \mathbf{K}_{em}^{u\alpha} &= \mathbf{K}_{em}^{\alpha u} = \int_{\Omega^{[e]}} (\mathbf{B}_I^u)^T \beta \mathbf{B}_J^\alpha d\Omega; \\ \mathbf{K}_{em}^{u\beta} &= \mathbf{K}_{em}^{\beta u} = \int_{\Omega^{[e]}} (\mathbf{B}_I^u)^T \beta \mathbf{B}_J^\beta d\Omega; \\ \mathbf{K}_{em}^{\alpha\alpha} &= \int_{\Omega^{[e]}} (\mathbf{B}_I^\alpha)^T \beta \mathbf{B}_J^\alpha d\Omega; \\ \mathbf{K}_{em}^{\alpha\beta} &= \mathbf{K}_{em}^{\beta\alpha} = \int_{\Omega^{[e]}} (\mathbf{B}_I^\alpha)^T \beta \mathbf{B}_J^\beta d\Omega; \\ \mathbf{K}_{em}^{\beta\beta} &= \int_{\Omega^{[e]}} (\mathbf{B}_I^\beta)^T \beta \mathbf{B}_J^\beta d\Omega \end{aligned} \quad (A.7)$$

$$\begin{aligned} \mathbf{K}_{me}^{uu} &= \mathbf{K}_{em}^{uu}; \quad \mathbf{K}_{me}^{u\alpha} = \mathbf{K}_{em}^{\alpha u} = \mathbf{K}_{em}^{u\alpha} = \mathbf{K}_{em}^{\alpha u}; \\ \mathbf{K}_{me}^{u\beta} &= \mathbf{K}_{em}^{\beta u} = \mathbf{K}_{em}^{u\beta} = \mathbf{K}_{em}^{\beta u}; \quad \mathbf{K}_{me}^{\alpha\alpha} = \mathbf{K}_{em}^{\alpha\alpha}; \\ \mathbf{K}_{me}^{\alpha\beta} &= \mathbf{K}_{em}^{\beta\alpha} = \mathbf{K}_{em}^{\beta\alpha} = \mathbf{K}_{em}^{\beta\alpha}; \quad \mathbf{K}_{me}^{\beta\beta} = \mathbf{K}_{em}^{\beta\beta} \end{aligned} \quad (A.8)$$

$$\begin{aligned} \mathbf{K}_{m\bar{m}}^{uu} &= \int_{\Omega^{[e]}} (\mathbf{B}_I^u)^T \gamma \mathbf{B}_J^u d\Omega; \\ \mathbf{K}_{m\bar{m}}^{u\alpha} &= \mathbf{K}_{m\bar{m}}^{\alpha u} = \int_{\Omega^{[e]}} (\mathbf{B}_I^u)^T \gamma \mathbf{B}_J^\alpha d\Omega; \\ \mathbf{K}_{m\bar{m}}^{u\beta} &= \mathbf{K}_{m\bar{m}}^{\beta u} = \int_{\Omega^{[e]}} (\mathbf{B}_I^u)^T \gamma \mathbf{B}_J^\beta d\Omega; \\ \mathbf{K}_{m\bar{m}}^{\alpha\alpha} &= \int_{\Omega^{[e]}} (\mathbf{B}_I^\alpha)^T \gamma \mathbf{B}_J^\alpha d\Omega; \\ \mathbf{K}_{m\bar{m}}^{\alpha\beta} &= \mathbf{K}_{m\bar{m}}^{\beta\alpha} = \int_{\Omega^{[e]}} (\mathbf{B}_I^\alpha)^T \gamma \mathbf{B}_J^\beta d\Omega; \\ \mathbf{K}_{m\bar{m}}^{\beta\beta} &= \int_{\Omega^{[e]}} (\mathbf{B}_I^\beta)^T \gamma \mathbf{B}_J^\beta d\Omega \end{aligned} \quad (A.9)$$

References

- Bechet, E., Minnebo, H., Moes, N., et al., 2005. Improved implementation and robustness study of the X-FEM for stress analysis around cracks. Int. J. Numer. Meth. Eng. 64, 1033–1056.
- Benson, D.J., Bazilevs, Y., De Luycker, E., et al., 2010. A generalized finite element formulation for arbitrary basis functions: From isogeometric analysis to XFEM. Int. J. Numer. Meth. Eng. 83, 765–785.
- Bhardwaj, G., Singh, I.V., Mishra, B.K., 2015. Stochastic fatigue crack growth simulation of interfacial crack in bi-layered FGMs using XIGA. Comput. Meth. Appl. Mech. Eng. 284, 186–229.
- Bhardwaj, G., Singh, I.V., Mishra, B.K., et al., 2015. Numerical simulation of functionally graded cracked plates using NUBRS based XIGA under different loads and boundary conditions. Compos. Struct. 126, 347–359.

- Bhattacharya, S., Singh, I.V., Mishra, B.K., et al., 2013. Fatigue crack growth simulations of interfacial cracks in bi-layered FEMs using XFEM. *Comput. Mech.* 52, 799–814.
- Bui, Q.T., Zhang, C.H., 2012. Extended finite element simulation of stationary dynamic cracks in piezoelectric solids under impact loading. *Comput. Mater. Sci.* 62, 243–257.
- Bui, Q.T., Zhang, C.H., 2013. Analysis of generalized dynamic intensity factors of cracked magnetoelastic solids by X-FEM. *Finite Elem. Anal. Des.* 69, 19–36.
- Bui, Q.T., Nguyen, N.M., Zhang, C.H., 2011. A moving Kriging interpolation-based element-free Galerkin method for structural dynamic analysis. *Comput. Meth. Appl. Mech. Eng.* 200, 1354–1366.
- Bui, Q.T., Khosravifard, Z.C., Hematiyan, M.R., et al., 2013. Dynamic analysis of sandwich beams of functionally graded core using a truly meshfree radial point interpolation method. *Eng. Struct.* 47, 90–104.
- Bui, Q.T., 2015. Extended isogeometric dynamic and static fracture analysis for cracks in piezoelectric materials using NURBS. *Comput. Meth. Appl. Mech. Eng.* 295, 470–509.
- Corral-Flores, V., Bueno-Baques, D., Ziolo, R.F., 2010. Synthesis and characterization of novel $\text{CoFe}_2\text{O}_4\text{-BaTiO}_3$ multiferroic core-shell-type nanostructures. *Acta Mater.* 58, 764–769.
- Cottrell, J.A., Hughes, T.J.R., Bazilevs, Y., 2009. Isogeometric Analysis: Toward Integration of CAD and FEA. John Wiley & Sons, UK.
- De Luycker, E., Benson, D.J., Belytschko, T., et al., 2011. X-FEM in isogeometric analysis for linear fracture mechanics. *Int. J. Numer. Meth. Eng.* 87, 541–565.
- Dolbow, J., 1999. An Extended Finite Element Method with Discontinuous Enrichment for Applied Mechanics. Theoretical and Applied Mechanics (Ph.D dissertation). Northwestern University, Evanston, IL, USA.
- Feng, W.J., Pan, E., 2008. Dynamic fracture behavior of an internal interfacial crack between two dissimilar magneto-electro-elastic plates. *Eng. Fract. Mech.* 75, 1468–1487.
- Feng, W.J., Pan, E., Wang, X., 2007. Dynamic fracture analysis of a penny-shaped crack in a magnetoelastic layer. *Int. J. Solids Struct.* 44, 7955–7974.
- Fleming, M., Chu, Y.A., Moran, B., et al., 1997. Enriched element-free Galerkin methods for crack tip fields. *Int. J. Numer. Meth. Eng.* 40, 1483–1504.
- Ghorashi, S.S., Valizadeh, V., Mohammadi, S., 2011. Extended isogeometric analysis for simulation of stationary and propagating cracks. *Int. J. Numer. Meth. Eng.* 89, 1069–1101.
- Ghorashi, S.S., Valizadeh, V., Mohammadi, S., et al., 2015. T-spline based XIGA for fracture analysis of orthotropic media. *Comput. Struct.* 147, 138–146.
- Hughes, T.J.R., Cottrell, J.A., Bazilevs, Y., 2005. Isogeometric analysis: CAD, finite elements, NURBS, exact geometry and mesh refinement. *Comput. Meth. Appl. Mech. Eng.* 194, 4135–4195.
- Laborde, P., Pommier, J., Renard, Y., et al., 2005. High-order extended finite element method for cracked domains. *Int. J. Numer. Meth. Eng.* 64, 354–381.
- Lei, J., Ch, Z., Bui, Q.T., 2015. Transient dynamic interface crack analysis in magnetoelastic bi-materials by a time-domain BEM. *Eur. J. Mech. – A/Solids* 49, 146–157.
- Lei, J., Sun, P., Bui, Q.T., 2015. Determination of fracture parameters for interface cracks in transverse isotropic magnetoelastic composites. *Curved Layer. Struct.* 2, 271–278.
- Li, Y.S., Feng, W.J., Xu, Z.H., 2009. Fracture analysis of cracked 2D planar and axisymmetric problems of magneto-electro-elastic materials by the MLPG coupled with FEM. *Comput. Mech. Appl. Mech. Eng.* 198, 2347–2359.
- Liu, Y.X., Wang, J.G., Liu, J.M., et al., 2003. Effect of magnetic bias field on magnetoelectric coupling in magnetolectric composites. *J. Appl. Phys.* 94, 5118–5122.
- Liu, P., Yu, T.T., Bui, Q.T., et al., 2013. Transient dynamic crack analysis in non-homogeneous functionally graded piezoelectric materials by the X-FEM. *Comput. Mater. Sci.* 69, 542–558.
- Liu, P., Yu, T.T., Bui, Q.T., et al., 2014. Transient thermal shock fracture analysis of functionally graded piezoelectric materials by the extended finite element method. *Int. J. Solids Struct.* 51, 2167–2182.
- Liu, P., Bui, Q.T., Zhu, D., et al., 2015. Buckling failure analysis of cracked functionally graded plates by a stabilized discrete shear gap extended 3-node triangular plate element. *Compos. Part B* 77, 179–193.
- Nam, C.W., 1994. Magnetoelectric effect in composites of piezoelectric and piezomagnetic phases. *Phys. Rev. B* 50, 6082–6088.
- Nanthakumar, S.S., Lahmer, T., Rabczuk, T., 2013. Detection of flaws in piezoelectric structures using extended FEM. *Int. J. Numer. Meth. Eng.* 96, 373–389.
- Nanthakumar, S.S., Lahmer, T., Rabczuk, T., 2014. Detection of multiple flaws in piezoelectric structures using XFEM and level sets. *Comput. Meth. Appl. Mech. Eng.* 275, 98–112.
- Nguyen, T.N., Bui, Q.T., Zhang, C.H., et al., 2014. Crack growth modeling in elastic solids by the extended meshfree Galerkin radial point interpolation method. *Eng. Anal. Bound. Elem.* 44, 87–97.
- Nguyen, N.M., Bui, Q.T., Yu, T.T., et al., 2014. Isogeometric analysis for unsaturated flow problems. *Comput. Geotech.* 62, 257–267.
- Piegl, L., Tiller, W., 1995. The NURBS Book. Springer, Berlin Heidelberg.
- Prange, C., Loehnert, S., Wriggers, P., 2012. Error estimation for crack simulations using the XFEM. *Int. J. Numer. Meth. Eng.* 91, 1459–1474.
- Racz, D., Bui, Q.T., 2012. Novel adaptive meshfree integration techniques in meshless methods. *Int. J. Numer. Meth. Eng.* 90, 1414–1434.
- Rajapakse, R.K.N.D., 1997. Plane strain/stress solutions for piezoelectric solids. *Compos. Part B* 28, 385–396.
- Rao, B.N., Kuna, M., 2008. Interaction integrals for fracture analysis of functionally graded magnetoelastic materials. *Int. J. Fract.* 153, 15–37.
- Riley, J.D., 1955. Solving systems of linear equations with a positive definite, symmetric, but possibly ill-conditioned matrix. *Math. Tables Other Aids Comput.* 9, 96–101.
- Rojas-Díaz, R., Saez, A., García-Sánchez, F., et al., 2008. Time-harmonic Green's functions for anisotropic magnetoelasticity. *Int. J. Solids Struct.* 45, 144–158.
- Rojas-Díaz, R., García-Sánchez, F., Saez, A., et al., 2009. Dynamic crack interactions in magnetoelastic composite materials. *Int. J. Fract.* 157, 119–130.
- Rojas-Díaz, R., García-Sánchez, F., Saez, A., 2010. Analysis of cracked magnetoelastic composites under time-harmonic loading. *Int. J. Solids Struct.* 47, 71–80.
- Rojas-Díaz, R., García-Sánchez, F., Saez, A., et al., 2011. Fracture analysis of plane piezoelectric/piezomagnetic multiphase composites under transient loading. *Comput. Meth. Appl. Mech. Eng.* 200, 2931–2942.
- Rojas-Díaz, R., Sukumar, N., Saez, A., et al., 2011. Fracture in magnetoelastic materials using the extended finite element method. *Int. J. Numer. Meth. Eng.* 88, 1238–1259.
- Sharma, K., Bui, Q.T., Zhang, C.H., et al., 2013. Analysis of a subinterface crack in piezoelectric bimaterials with the extended finite element method. *Eng. Fract. Mech.* 104, 114–139.
- Shojaee, S., Valizadeh, N., Izadpanah, E., et al., 2012. Free vibration and buckling analysis of laminated composite plates using the NURBS-based isogeometric finite element method. *Compos. Struct.* 94, 677–693.
- Sladek, J., Sladek, V., Solek, P., et al., 2008. Fracture analysis of cracks in magneto-electro-elastic solids by the MLPG. *Comput. Mech.* 42, 697–714.
- Sladek, J., Sladek, V., Solek, P., et al., 2010. Fracture analysis in continuously nonhomogeneous magneto-electro-elastic solids under a thermal load by the MLPG. *Int. J. Solids Struct.* 47, 1381–1391.
- Sladek, J., Sladek, V., Zhang, C.H., et al., 2012. Semi-permeable crack analysis in magnetoelastic solids. *Smart Mater. Struct.* 21, 025003.
- Song, Z.F., Sih, G.C., 2003. Crack initiation behavior in a magnetoelastic composite under in-plane deformation. *Theor. Appl. Fract. Mech.* 39, 189–207.
- Strouboulis, T., Babuska, I., Copps, K., 2000. The design and analysis of the generalized finite element method. *Int. J. Numer. Meth. Eng.* 181, 43–69.
- Valizadeh, N., Natarajan, S., Gonzalez-Estrada, O., et al., 2013. NURBS-based finite element analysis of functionally graded plates: Static bending, vibration, buckling and flutter. *Compos. Struct.* 99, 309–326.
- Valizadeh, N., Bui, Q.T., Vu, V.T., et al., 2013. Isogeometric simulation for buckling, free and forced vibration of orthotropic plates. *Int. J. Appl. Mech.* 05, 1350017.
- Wünsche, M., Saez, A., García-Sánchez, F., et al., 2012. Transient dynamic crack analysis in linear magnetoelastic solids by a hypersingular time-domain BEM. *Eur. J. Mech. – A/Solids* 32, 118–130.
- Wünsche, M., Zhang, C.H., Sladek, J., et al., 2013. The influences of non-linear electrical, magnetic and mechanical boundary conditions on the dynamic intensity factors of magnetoelastic solids. *Eng. Fract. Mech.* 97, 297–313.
- Wang, B.L., Mai, Y.W., 2007. Self-consistent analysis of coupled magnetoelastic fracture – theoretical investigation and finite element verification. *Comput. Meth. Appl. Mech. Eng.* 196, 2044–2054.
- Wang, D.D., Xuan, J.C., 2010. An improved NURBS-based isogeometric analysis with enhanced treatment of essential boundary conditions. *Comput. Meth. Appl. Mech. Eng.* 199, 2425–2436.
- Yin, S.H., Hale, J.S., Yu, T.T., et al., 2014. Isogeometric locking-free plate element: A simple first order shear deformation theory for functionally graded plates. *Compos. Struct.* 118, 121–138.

- Yin, S.H., Yu, T.T., Bui, Q.T., et al., 2015. A cutout isogeometric analysis for thin laminated composite plates using level sets. *Compos. Struct.* 127, 152–164.
- Yin, S.H., Yu, T.T., Bui, Q.T., et al., 2015. Geometrically nonlinear analysis of functionally graded plates using isogeometric analysis. *Eng. Comput.* 32, 519–558.
- Yu, H.J., Wu, L.Z., Li, H., 2014. A domain-independent integration integral for magneto-electro-elastic materials. *Int. J. Solids Struct.* 51, 336–351.
- Yu, T.T., Bui, Q.T., Liu, P., et al., 2015. Interfacial dynamic impermeable cracks analysis in dissimilar piezoelectric materials under coupled electromechanical loading with the extended finite element method. *Int. J. Solids Struct.* 67, 205–218.
- Yu, T.T., Bui, Q.T., Liu, P., 2016a. A stabilized discrete shear gap extended finite element for the analysis of cracked Reissner-Mindlin plate vibration problems involving distorted meshes. *Int. J. Mech. Mater. Des* 12, 85–107.
- Yu, T.T., Bui, Q.T., Yin, S.H., et al., 2016b. On the thermal buckling analysis of functionally graded plates with internal defects using extended isogeometric analysis. *Compos. Struct.* 136, 684–695.
- Yu, T.T., Yin, S.H., Bui, Q.T., et al., 2016c. NURBS-based isogeometric analysis of buckling and free vibration problems for laminated composites plates with complicated cutouts using a new simple FSDT theory and level set method. *Thin-Walled Struct.* 101, 141–156.
- Yu, T.T., Yin, S.H., Bui, Q.T., et al., 2015. A simple FSDT-based isogeometric analysis for geometrically nonlinear analysis of functionally graded plates. *Finite Elem. Anal. Des.* 96, 1–10.
- Zhang, X.D., Bui, Q.T., 2015. A fictitious crack XFEM with two new solution algorithms for cohesive crack growth modeling in concrete structures. *Eng. Comput.* 32, 473–497.
- Zhong, X.C., Li, X.F., Lee, K.Y., 2009. Transient response of a cracked magnetoelectric material under the action of in-plane sudden impacts. *Comput. Mater. Sci.* 45, 905–911.
- Zhong, X.C., Liu, F., Li, X.F., 2009. Transient response of a magnetoelectroelastic solid with two collinear dielectric cracks under impacts. *Int. J. Solids Struct.* 46, 2950–2958.
- Zhou, Z.G., Wu, L.Z., Wang, B., 2005. The dynamic behavior of two collinear interface cracks in magneto-electro-elastic materials. *Eur. J. Mech. A/Solids* 24, 253–262.